HEALTH AND MEDICINE

# Hypothyroidism confers tolerance to cerebral malaria

**Diego Rodriguez-Muñoz[1], Ángela Sánchez[1], Susana Pérez-Benavente[2], Constanza Contreras-Jurado[3,4], Ana Montero-Pedrazuela[3], Marta Toledo-Castillo[1], María Gutiérrez-Hernández[1], Raquel Rodrigues-Díez[5,6], Cintia Folgueira[7], Ana M. Briones[5,6], Guadalupe Sabio[7], Ignacio Monedero-Cobeta[8], Irene Chávez-Coira[9], David Castejón[10], Encarnación Fernández-Valle[10], Javier Regadera[9], José M. Bautista[2], Ana Aranda[3,11,12]*, Susana Alemany[1,11]***



**The modulation of the host's metabolism to protect tissue from damage induces tolerance to infections increasing survival. Here, we examined the role of the thyroid hormones, key metabolic regulators, in the outcome of malaria. Hypothyroidism confers protection to experimental cerebral malaria by a disease tolerance mechanism. Hypothyroid mice display increased survival after infection with *Plasmodium berghei* ANKA, diminishing intracranial pressure and brain damage, without altering pathogen burden, blood-brain barrier disruption, or immune cell infiltration. This protection is reversed by treatment with a Sirtuin 1 inhibitor, while treatment of euthyroid mice with a Sirtuin 1 activator induces tolerance and reduces intracranial pressure and lethality. This indicates that thyroid hormones and Sirtuin 1 are previously unknown targets for cerebral malaria treatment, a major killer of children in endemic malaria areas.**

## INTRODUCTION

Malaria, caused by *Plasmodium falciparum*, is a devastating disease that results in the infection of millions of people each year (*1*) (www.who.int/teams/global-malaria-programme/reports/). Cerebral malaria (CM), which affects mainly children under the age of 5, is the most lethal form of the disease (*2*). CM is characterized by disruption of the blood-brain barrier (BBB), brain swelling leading to an increase in intracranial pressure (ICP) with compression of cerebral vessels, and hemorrhaging, which causes altered consciousness, seizures, paralysis, coma, and ultimately death. Infection with *Plasmodium berghei* ANKA (PbA) strain in C57BL/6 mice is widely used as a model of experimental CM (ECM), recapitulating the progression of CM in humans (*3*). Control of infections involves not only pathogen clearance by activation of the immune system but also disease tolerance (*4*), which enables the host tissues to limit the consequences of the infection without interfering directly with the host's pathogen load (*5*). Metabolic reprogramming is required for disease tolerance, diminishing tissue damage, and maintaining homeostatic parameters within a dynamic range compatible with the host survival (*6*). The master regulators of metabolism Sirtuin 1 (Sirt1), adenosine monophosphate–activated protein kinase (AMPK), and mammalian target of rapamycin complex 1 (mTORC1) are key energy sensors that respond to energy, nutrient, and stress stimuli. Sirt1 increases energy expenditure (*7*, *8*) and is associated with metabolic and age-related health benefits (*9*, *10*). AMPK plays a key role in the regulation of protein and lipid metabolism in response to changes in fuel availability (*11*), and mTORC1 also controls many fundamental processes, from protein synthesis to autophagy (*12*).

Several disease tolerance mechanisms have been reported in the host response to malaria. The malaria survival advantage conferred by human hemoglobin variants (*13*) in a mice model of ECM with sickle cell trait has been shown to occur irrespective of parasite load (*14*). Dietary restriction (*15*), a high-fat diet (*16*, *17*), adrenal hormones (*18*), targeting glutamine metabolism with a glutamine analog (*19*), or inhibiting glycolysis (*20*) also protects against ECM, reinforcing the idea that the host metabolic state plays a major role in tolerance against this disease. One of the most recognized actions of the thyroid hormones (THs; thyroxine or T4 and triiodothyronine or T3) is the regulation of the metabolic cycles, increasing energy expenditure (*21*). THs regulate energy expenditure via the central nervous system (*22*–*24*) and through a direct role in the major metabolic tissues (*25*). Under conditions of severe infection, a decline of TH levels is a common phenomenon called the "euthyroid sick syndrome" or "nonthyroidal illness syndrome" (NTIS) (*26*), diminishing the metabolic rate of the host, which could represent an emergency response to the infection. Although it has been reported that thyroid gland function decreases during malaria infection (*27*, *28*), the role of the thyroidal status in experimental models of malaria has not yet been examined. Iodine deficiency is still today an important public health problem (*29*). In underdeveloped countries where malaria prevails, there are endemic areas of iodine deficiency and consequently of insufficient TH secretion, as iodine is an essential component of the TH molecule (see www.ign.org/cm_data/IGN_Global_Map_AllPop_30May2017.pdf and www.cdc.gov/malaria/about/distribution.html). Reduction of thyroid gland activity during malaria infection could aggravate the outcome of the disease, but it could also constitute a defense mechanism.

Here, we show that hypothyroidism confers tolerance to CM in mice, reducing ICP and increasing survival without altering pathogen load. Sirt1 is involved in this effect, since this protection is reversed by treatment with the Sirt1 inhibitor EX-527. Furthermore, treatment

[1]Departament of Metabolism and Cell Signaling, Instituto de Investigaciones Biomédicas Alberto Sols, Consejo Superior de Investigaciones Científicas, Universidad Autónoma de Madrid, Madrid, Spain. [2]Department of Biochemistry and Molecular Biology, Research Institute Hospital 12 de Octubre (Imas12), Universidad Complutense de Madrid, Madrid, Spain. [3]Department of Endocrine and Nervous System Pathophysiology, Instituto de Investigaciones Biomédicas Alberto Sols, Consejo Superior de Investigaciones Científicas, Universidad Autónoma de Madrid, Madrid, Spain. [4]Departamento de Bioquímica, Facultad de Medicina, Universidad Alfonso X El Sabio, Villanueva de la Cañada, Madrid, Spain. [5]Departament of Pharmacology, Instituto de Investigación Hospital La Paz, Universidad Autónoma de Madrid, 28029 Madrid, Spain. [6]CIBER de Enfermedades Cardiovasculares, ISCIII, Madrid, Spain. [7]Departament of Myocardial Pathophysiology, Centro Nacional de Investigaciones Cardiovasculares, ISCIII, 28029 Madrid, Spain. [8]Department of Physiology, Universidad Autónoma de Madrid, Madrid, Spain. [9]Department of Anatomy, Histology and Neuroscience, Universidad Autónoma de Madrid, Madrid, Spain. [10]MNR Unit (CAI de Bioimagen), Universidad Complutense de Madrid, Madrid, Spain. [11]Biomedicine Unit (Unidad Asociada al CSIC), Universidad de Las Palmas de Gran Canaria, Las Palmas, Spain. [12]Centro de Investigación Biomédica en Red de Cáncer (CIBERONC), ISCIII, Madrid, Spain.
*Corresponding author. Email: aaranda@iib.uam.es (A.A.); salemany@iib.uam.es (S.A.)

of normal thyroid function mice with the Sirt1 activator SRT1720 mimics the effect of hypothyroidism, promoting tolerance and reducing ICP and lethality. Our findings suggest that targeting Sirt1 is a potential coadjuvant treatment for CM.

## RESULTS

### Hypothyroidism promotes survival in ECM

Infection with PbA of euthyroid mice caused 100% lethality at days 6 to 7 after infection. In contrast, more than 40% of hypothyroid mice receiving a low-iodine diet and antithyroidal drugs were still alive at day 15 (Fig. 1A). At day 5 after infection, all euthyroid mice presented ECM symptoms, including paralysis and ataxia (stage 3). At day 6, they usually suffered convulsions and coma (stage 4) before death, while infected hypothyroid mice presented no ECM symptoms (Fig. 1B and movies S1 and S2). About 40% of the hypothyroid mice never presented clear symptoms of ECM, but they eventually died from anemia at days 18 to 20 after infection (fig. S1A). Parasitemia levels were similar in both groups during the course of the infection (Fig. 1C), suggesting that hypothyroidism may confer tolerance to ECM. At day 6 after infection, both euthyroid and hypothyroid mice lost about 10% of body weight (BW; Fig. 1D), regardless of the fact that hypothyroid mice had a lower BW on the day of the infection, since hypothyroidism resulted in strongly reduced weight gain (fig. S1B). Infected euthyroid mice presented NTIS, with a marked decrease of total circulating T3 and T4 levels at day 6 after infection. Predictably, hypothyroid mice displayed a severe decrease of circulating THs at the times tested (Fig. 1E). In addition, the levels of hepatic *Deiodinase* I mRNA, a widely used readout of TH action (*30*), faithfully reproduced the levels of circulating hormones (fig. S1C).

Shifting euthyroid mice to hypothyroid diet at day 0, but not at day 3 of PbA infection, arrested ECM development, and animals survived (Fig. 1F). Switching of hypothyroid animals to control diet and treatment with TH in the drinking water at day 3 after infection accelerated their death, and when the switch was made on the same day of infection, they died on day 6. (Fig. 1G). Intracerebroventricular (ICV) administration of T3 to hypothyroid mice for 6 days also accelerated death and appearance of ECM symptoms. While more than 80% of the animals injected with vehicle survived at day 7, only 50% of the animals injected with T3 were alive at day 5 and 17% died as early as day 4. Once the treatment stopped, both groups showed a similar survival (Fig. 1H). These results suggest that the effects of the TH are at least partially exerted directly in the brain. In addition, omission of the antithyroidal drug $KClO_4$ did not reduce survival of hypothyroid mice, indicating that extremely severe hypothyroidism is not required for protection against ECM. Last, hyperthyroidism increased the sensitivity to ECM, as all hyperthyroid-infected mice died at day 5, 1 day earlier than the euthyroid mice (Fig. 1I). Adrenalectomy, which has been shown to enhance mortality in C57BL/6 mice infected with the parasite strains *P. berghei* Edinburgh (*Pb*NK65-E*Pb*NK65) or New York (*Pb*NK65-NY), accelerating death by hypoglycemia at days 7 to 10 after infection (*18*), did not alter lethality by PbA in euthyroid mice, which died at day 6 before developing strong hypoglycemia. In addition, adrenalectomy did not reverse the effect of hypothyroidism on increased survival (fig. S2). These data indicate that the thyroidal status plays an important role in the outcome of ECM. However, this TH-driven effect was lost in the outcome of non-CM caused by *Plasmodium yoelii* YM (Fig. 1, J and K) and did not render BALB/c mice susceptible to ECM when infected with PbA, as both euthyroid and hyperthyroid mice died without developing ECM symptoms (not illustrated).

### Enhanced splenic response in PbA-infected hypothyroid mice

Infected euthyroid and hypothyroid mice displayed similar hemograms (fig. S3, A and B), with the exception of a somewhat stronger reduction of red blood cell and platelet values in hypothyroid mice at day 6 after infection. Besides, infected hypothyroid mice showed increased levels of interferon-γ (IFN-γ) and CXCL-1, a tendency toward a higher circulating tumor necrosis factor–α (TNF-α), interleukin-1 (IL-6), and CCL-2, and a significant increase of IL-10 (fig. S3C). Circulating glucose levels were reduced in both groups to a similar extent upon infection (fig. S3D). Thus, hypothyroid mice show reduced severe ECM pathology despite having similar hemograms and glycemia, and a higher cytokine display than euthyroid mice.

Spleen is crucial for a proper immune response to malaria (*31*). Although hypothyroid mice displayed noticeable spleen atrophy, at day 6 after infection, they showed a marked splenomegaly, with a significantly higher increase in spleen size and weight than euthyroid mice (fig. S4A). Histological analysis of infected spleens from both groups showed the typical malaria infection appearance: abundant erythroid cells and hyperplastic lymphoid follicles with an extended infiltration into red pulp (fig. S4B). In parallel to splenic weight changes, uninfected hypothyroid mice displayed a reduced number of splenocytes, but at day 6 after infection, hypothyroid mice showed a stronger increase in splenic cellularity, including erythroid cells, than euthyroid mice (fig. S4C). Among the different late erythroblasts, gated as described in (*32*) and fig. S5 (A and B), infected hypothyroid mice showed a reduced number of Ery B with respect to the euthyroid mice, and Ery C supported in both groups the major increase at day 6 after infection (fig. S4D). Splenic leukocytes and different myeloid and T cell lineages included therein were reduced in the hypothyroid mice before infection and augmented significantly in these mice, but not in euthyroid mice, upon infection (fig. S4E). Before infection, the number of B cells was reduced in hypothyroid spleens, but increased in both groups after infection, reaching similar values (fig. S4F).

Expression of CD49d and CD11c (which defines the PbA-specific T cells) (*33*), of CXCR3 and CCR5 (chemokine receptors required for their migration to the brain) (*34*, *35*), of the activation marker CD69, of Granzyme B (required for the development of CM) (*36*), and of Ki67 (a marker of cell proliferation) revealed a rather similar activation state on splenic T helper and cytotoxic cells between euthyroid and hypothyroid mice before the infection and at day 6 after the PbA inoculation (figs. S6 and S7). Plasmacytoid dendritic cells showed increased expression of the activation marker CD86 in infected hypothyroid mice with respect to the euthyroid mice, a difference that could not be observed in type 1 conventional dendritic cells (fig. S8). All these data indicate that PbA infection compensates the spleen atrophy generated by hypothyroidism with a massive increase in the number of different splenic cell types with the expected activation state at the late ECM stage.

### Hypothyroidism does not prevent BBB disruption in ECM

Despite their reduced BW, hypothyroid mice maintained a normal brain weight (Fig. 2A). BBB breakdown is a hallmark of ECM (*2*), and hypothyroidism did not protect its integrity, as assessed by

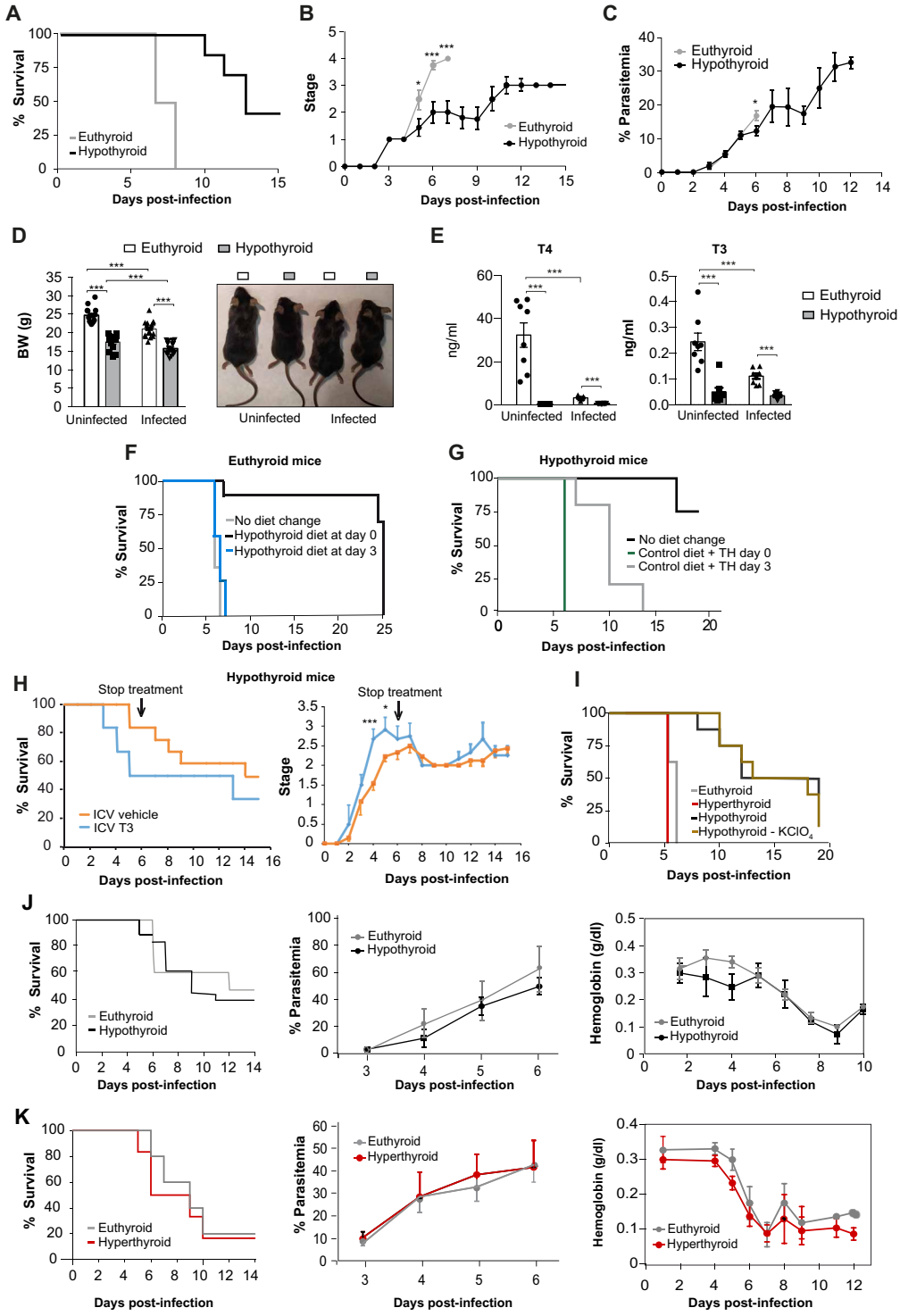


**Fig. 1. Hypothyroidism protects from ECM.** (**A**) Kaplan-Meier plot of euthyroid mice (fed a normal iodine diet) and hypothyroid mice (fed a low iodine diet with propylthiouracil and $KClO_4$ in the drinking water) infected with PbA ($n = 34, 36$). (**B**) Clinical stage of the mice ($n = 28, 34$). (**C**) Parasitemia expressed as % of infected erythrocytes ($n = 14$). (**D**) Body weight (BW) of euthyroid and hypothyroid mice at the day of PbA infection and at day 6 after infection ($n = 11$ to 13). (**E**) Total circulating T4 and T3 ($n = 8$ to 12). (**F**) Kaplan-Meier plot of euthyroid mice infected with PbA and shifted to hypothyroid treatment at days 0 and 3 after infection ($n = 7$ to 10). (**G**) Kaplan-Meier plot of hypothyroid mice infected with PbA and shifted to normal iodine diet and T4 and T3 treatment at days 0 and 3 after infection ($n = 5$). (**H**) Kaplan-Meier plot of hypothyroid-infected mice after daily intracerebroventricular (ICV) administration of vehicle or 16 ng of T3 for the first 6 days starting at day 0 of infection. Right: Clinical stage of the animals ($n = 12$ to 13). (**I**) Survival of PbA-infected mice with different thyroidal states: euthyroid, hypothyroid, hypothyroid diet without $KClO_4$, and hyperthyroid (normal iodine diet and T4 and T3 pretreatment for 14 days and maintained during the course of the infection, $n = 8$). (**J**) Kaplan-Meier plot ($n = 18, 15$), parasitemia ($n = 7$), and circulating hemoglobin ($n = 7$) of euthyroid and hypothyroid mice infected with *P. yoelii* YM. (**K**) Same parameters in hyperthyroid and euthyroid mice ($n = 5, 6$). In all panels, error bars represent means ± SEM [one-way analysis of variance (ANOVA) followed by multiple comparisons Tukey test]. $^*P < 0.05$ and $^{***}P < 0.001$.

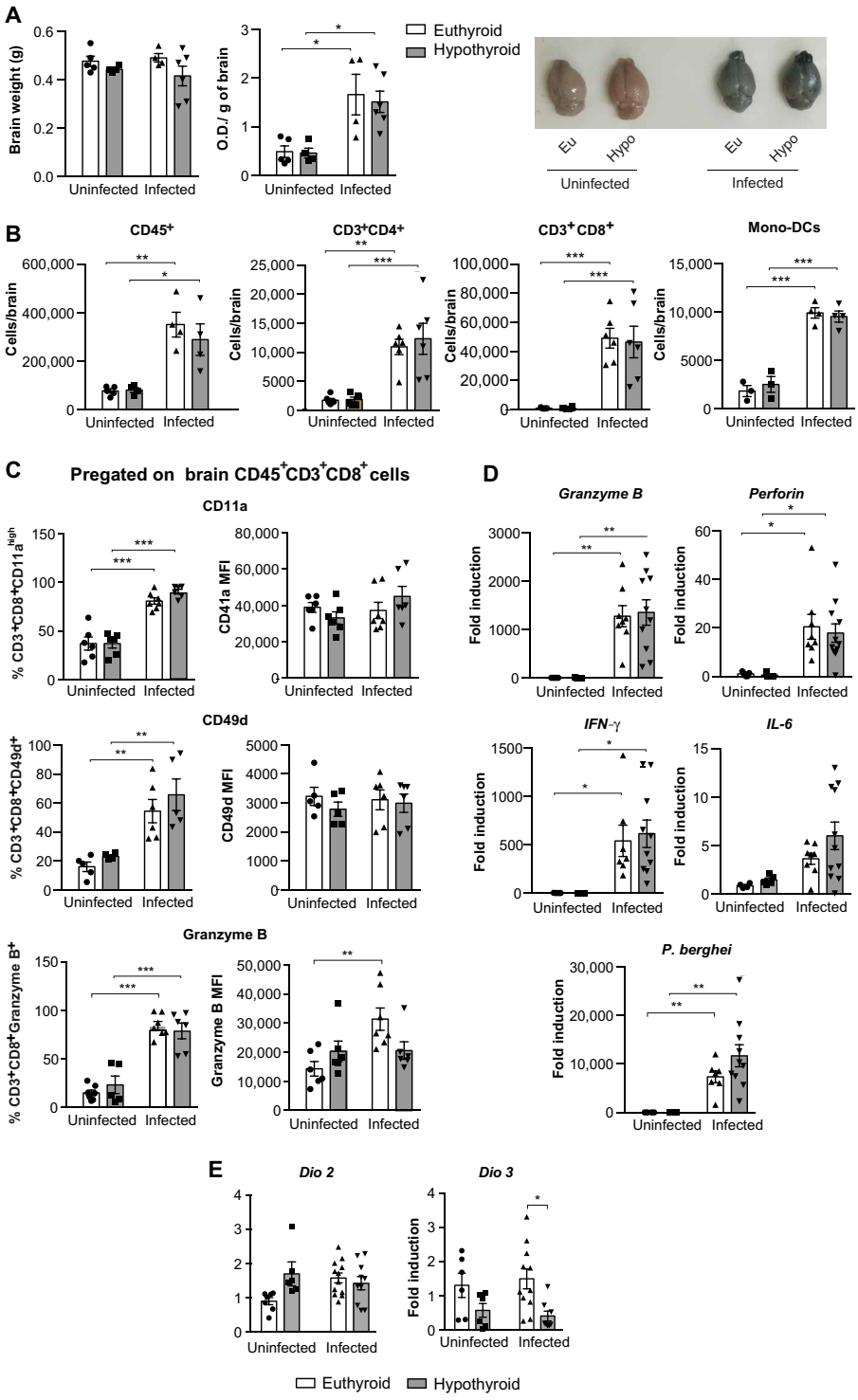


**Fig. 2. Hypothyroidism does not protect the integrity of the BBB.** (**A**) Brain weight, Evans blue staining ($n = 5$ to 6), and representative brain images of the uninfected mice and at day 6 after infection. O.D., optical density. (**B**) Number of brain-infiltrating leukocytes ($CD45^+$), T helper ($CD45^+CD3^+CD4^+$), T cytotoxic ($CD45^+CD3^+CD8^+$) lymphocytes, and monocyte-derived dendritic cells (Mono-DCs; $CD45^+F4/80^+CD11b^+CD206a^+MHCII^+$) ($n = 5$ to 7). (**C**) Percentage of cytotoxic T lymphocytes positive for CD11a, CD49d, and intracellular Granzyme B expression, and their corresponding mean fluorescence intensity (MFI) values ($n = 5$ to 6). (**D**) Levels of the indicated transcripts in the brains ($n = 5$ to 6). (**E**) Levels of brain *Deiodinase* 2 and 3 transcripts ($n = 6$ to 12). In all panels, error bars represent ±SEM, one-way ANOVA followed by multiple comparisons Tukey test. $^*P < 0.05$, $^{**}P < 0.01$, and $^{***}P < 0.001$.

extravasation of Evans blue 1 hour after intravenous injection at day 6 after PbA infection (Fig. 2A). Analysis by magnetic resonance imaging (MRI) after 15 min of an intraperitoneal injection of a contrast agent based on gadolinium also revealed BBB disruption in infected hypothyroid mice, although some quantitative differences in discrete areas with respect to the euthyroid mice were observed. Thus, while signal intensity was similar in cerebellum, hypothalamus, or hippocampus of infected euthyroid and hypothyroid mice, in other regions values were lower in the hypothyroid animals (fig. S9). The total number of brain-infiltrated helper and cytotoxic T lymphocytes, and monocyte-derived dendritic cells, identified as indicated in fig. S5 (C and D), was similar in infected euthyroid and hypothyroid mice (Fig. 2B). In addition, the percentage of $CD3^+CD8^+$ cells positive for CD11a, CD49d, and Granzyme B showed a similar increase in both groups, suggesting a comparable activation state (Fig. 2C). Brain mRNA levels of *granzyme B* and *perforin* also showed an analogous induction, and analysis of *IL-6* and *IFN-γ* transcripts revealed a similar pro-inflammatory microenvironment in the brain of both groups of infected mice. In addition, no significant differences between euthyroid and hypothyroid mice in the levels of *PbA* mRNA were found (Fig. 2D). All these data confirm BBB disruption and similar infiltration of leukocytes and entry of parasites into the brain in both groups of mice. Brain hypothyroidism was characterized by a tendency toward an increase in transcript levels of *Deiodinase* 2 before infection, which regulate the generation of T3 from T4, as well as with a reduction of *Deiodinase* 3 transcripts, the enzyme responsible for T3 degradation (Fig. 2E).

### Hypothyroidism protects from ECM-induced swelling and brain damage

ECM is associated with brain swelling and parenchymal lesions (*37*). T2-weighted MR images of the olfactory bulb, which plays a key role in the pathogenesis of ECM (*38*), showed the existence of hypointense areas (compatible with microhemorrhages) accompanied by hyperintensity (edema) in the central area in all infected euthyroid mice, but not in hypothyroid mice (Fig. 3A). Hematoxylin and eosin (H&E)–stained sections of the whole brain corroborated that infected euthyroid mice exhibited a significantly higher number of microhemorrhages (Fig. 3B). In infected euthyroid mice, but in none of the hypothyroid mice, edema was also propagated from the bulb to the rostral migratory stream, the subventricular zone, and the dorsal migratory stream, reaching the striatum and the corpus callosum and causing brain thickening (Fig. 3C).

Crushing of the cerebellum and brainstem herniation as a consequence of brain edema is considered to be a major cause of death in ECM (*37*) and in children with CM (*39*). PbA infection significantly increased brain volume and the cerebral area in euthyroid but not in hypothyroid mice (Fig. 3D). To quantify changes due to edema, the distances illustrated in Fig. 3D were measured in mid-sagittal T2-weighted images. While total brain length was not altered by infection (line 1), brain thickness (line 2) augmented in the euthyroid mice upon infection without changing in the hypothyroid mice. Brain compression also led to a change in the shape of the cerebellum in euthyroid but not in hypothyroid mice, as cerebellar length (line 3) increased, while cerebellar width (line 4) was reduced upon infection only in euthyroid animals. The distance from the pituitary gland to the anterior and posterior end of the cerebellum (lines 5 and 6) was also longer after PbA infection in euthyroid mice without changing in hypothyroid mice. These results confirm that significant compression, as a consequence of brain swelling, did not happen in hypothyroid mice that showed resistance to ECM. Visual inspection of the brain images (Fig. 3E) shows not only crushing of the cerebellum and the pituitary gland in the infected euthyroid mice but also engulfment of the brainstem into the foramen magnum.

### Hypothyroidism protects from increased ICP and cerebral blood flow damage

The above results are compatible with reduced ICP in infected hypothyroid mice when compared with infected euthyroid mice. An increase in ICP directly and proportionally affects the perioptic nerve space, causing an enlargement of the optic nerve diameter (*40*). PbA infection significantly increased ICP in euthyroid but not in hypothyroid mice (Fig. 4A). These changes appear to be independent of effects on peripheral blood pressure that was lower in the hypothyroid mice before infection and was reduced upon infection, reaching similar levels in both groups of mice (Fig. 4B). Mannitol has been proposed as an adjuvant to treat brain edema in CM (*41*). However, daily administration of mannitol, starting the day of infection, did not increase survival and did not modify the clinical score in infected euthyroid and hyperthyroid mice. Furthermore, mannitol was ineffective in reducing ICP or neurological symptoms in infected euthyroid mice (fig. S10).

Fatal outcome in ECM is also associated with compression of the cerebral vessels and impairment of the cerebral blood flow (CBF) as a consequence of brain swelling and increased ICP (*37*). Angiographies showed that uninfected hypothyroid mice displayed a markedly reduced CBF in coronal, axial, and sagittal images (Fig. 4C), which to our knowledge has not been previously reported. In parallel with increased ICP, infected euthyroid mice showed strong collapse of cerebral vessels and a significant reduction of the CBF. In contrast, CBF maps were quite similar in uninfected and infected hypothyroid mice (Fig. 4C and movie S3), which agrees with the absence of brain compression. Thus, hypothyroidism markedly reduces brain damage, precluding ICP increase and maintaining the CBF in PbA-infected mice without preventing BBB breakdown and parasite and leukocyte infiltration into the brain. Shifting euthyroid mice to hypothyroid diet at day 0 of PbA infection was sufficient to prevent brain vessel collapse, reducing ECM stage and increasing survival, while CBF was similarly reduced in euthyroid mice at day 6 and in hyperthyroid mice at day 5 after infection (fig. S11).

### Hypothyroid mice display altered brain metabolic profile after PbA infection

To analyze whether brain metabolic changes could be involved in the different outcomes of the disease in euthyroid and hypothyroid mice, we next conducted an analysis of brain aqueous low–molecular weight metabolites by nuclear MR spectroscopy before infection and at day 6 after infection. Clustering analysis showed that, before infection, hypothyroid brains display metabolic differences with respect to the euthyroid brains, with a predominance of underexpressed metabolites. In euthyroid mice, infection resulted in underexpression of multiple metabolites, whereas in hypothyroid mice a general increase was observed. Furthermore, upon infection, a distinct clustering of euthyroid and hypothyroid samples was observed, with increase in various metabolites in the hypothyroid animals that was not detected in euthyroid mice (Fig. 5A). We observed statistically significant differences in 22 metabolites, with a distinct profile depending on the thyroidal status and the infection

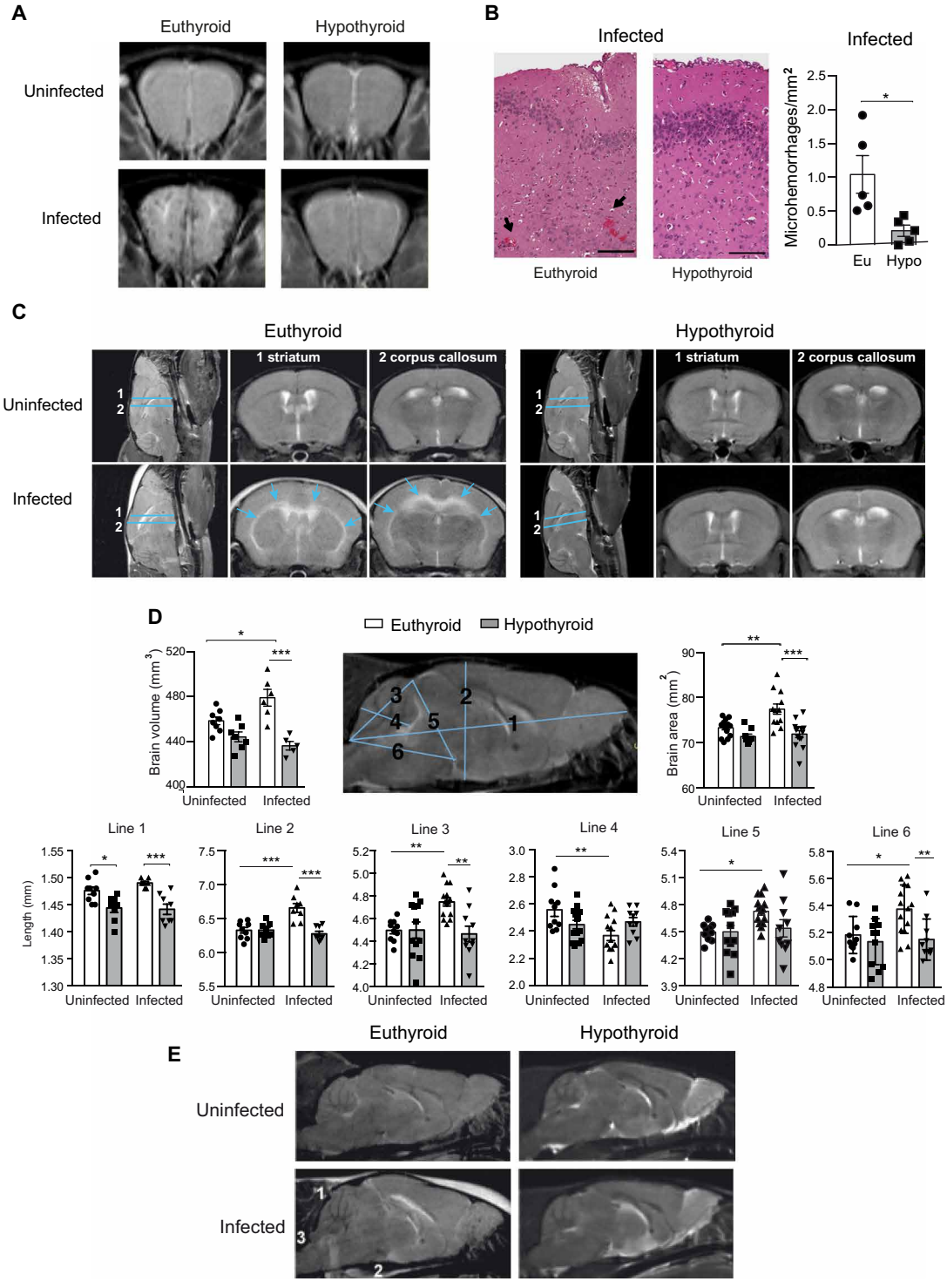


**Fig. 3. Brain damage and inflammation are reduced in infected hypothyroid mice.** (**A**) Representative olfactory bulb–axial T2-weighted MR images in euthyroid and hypothyroid uninfected mice and at day 6 after infection. (**B**) Representative H&E staining at ×100 of the cerebral cortex and number of microhemorrhages per square millimeter of total cerebral tissue. Means ± SEM, unpaired *t* test. $n = 6$. Scale bars, 1 mm. (**C**) Representative T2-weighted axial images of the brain regions indicated by lines 1 and 2 in the sagittal images, corresponding to the striatum and corpus callosum, of euthyroid and hypothyroid mice uninfected and 6 days after infection. Edema, characterized by the presence of hyperintense areas, is shown with arrows. (**D**) Brain volume, measured from T2-weighted MR images. Means ± SEM, $n = 5$ to 7, one-way ANOVA followed by multiple comparisons Tukey test. Midsagittal T2-weighted MR image showing lines 1 to 6 used to measure cerebral and cerebellar distances in euthyroid and hypothyroid mice uninfected and at day 6 after infection. Cerebral area was calculated from the ellipse determined by lines 1 and 2. Means ± SEM, $n = 10$ to 14, one-way ANOVA followed by multiple comparisons Tukey test. *$P < 0.05$, **$P < 0.01$, ***$P < 0.001$. (**E**) Representative images showing crushing of the cerebellum (1) and the pituitary gland (2) as well as brainstem herniation (3) only in infected euthyroid mice.

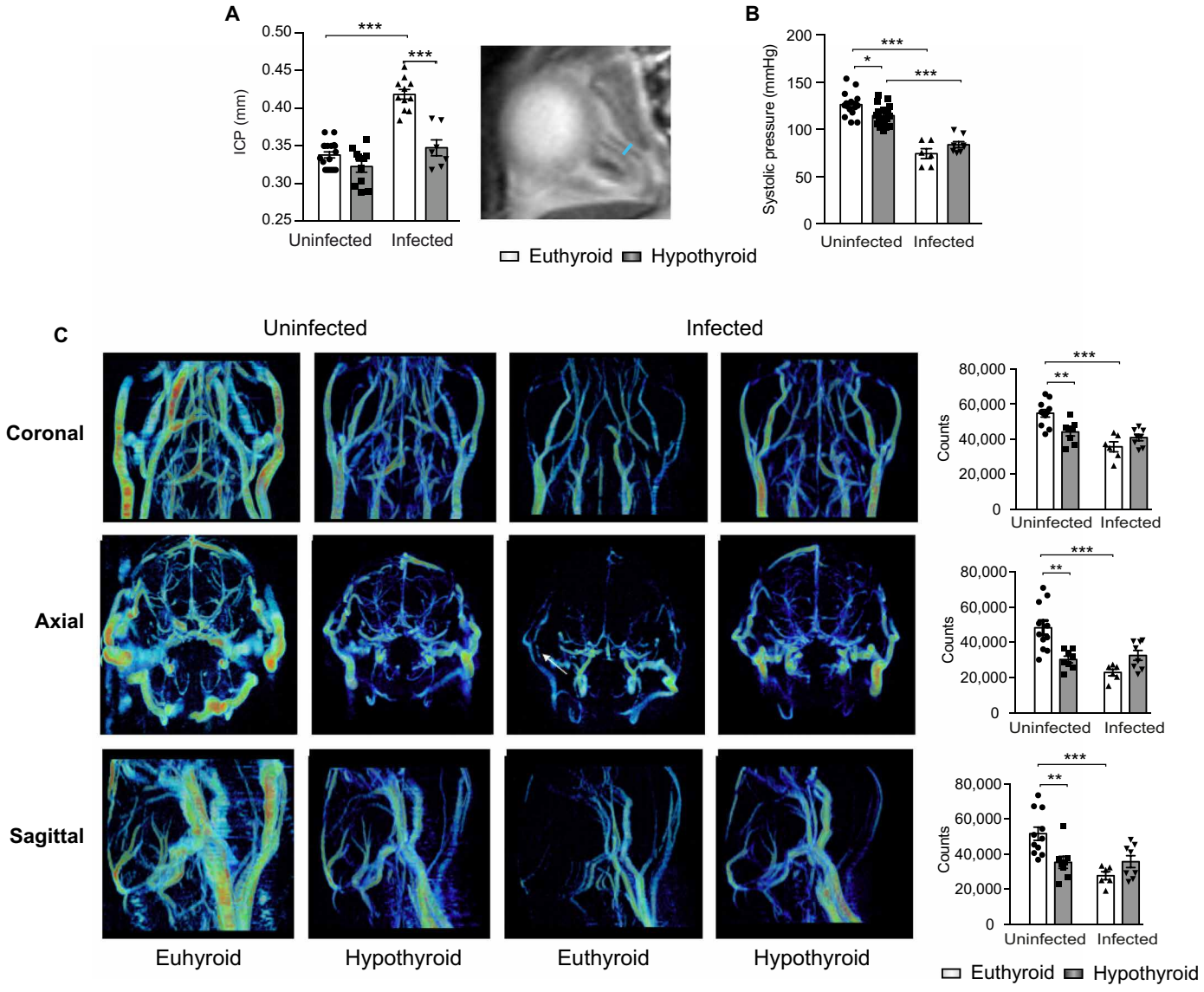


**Fig. 4. Hypothyroidism protects from increased intracraneal pressure and brain vessel compression.** (**A**) Intracranial pressure (ICP) in euthyroid and hypothyroid uninfected mice and at day 6 after infection. A representative T2-weighted image used for measurement of the nerve sheath diameter is shown at the right ($n = 7$ to 18). (**B**) Systolic blood pressure in the same animals ($n = 6$ to 18). (**C**) Representative coronal, axial, and sagittal maximum intensity projections of a three-dimensional time-of-flight angiogram and quantification of the angiograms in euthyroid and hypothyroid mice not infected and at day 6 after infection and quantification of signal intensity ($n = 7$ to 11). (A to C) Means ± SEM, one-way ANOVA followed by multiple comparisons Tukey test. *$P < 0.05$, **$P < 0.01$, and ***$P < 0.001$.

(fig. S12). The metabolic changes indicated a more efficient anaerobic metabolism in infected hypothyroid mice with a higher increase in the levels of lactate and a more efficient energy production with higher creatine levels (*42*, *43*). A significant increase in glutamine levels was observed upon infection in euthyroid and hypothyroid brains, but in hypothyroid mice, the levels of *N*-acetylaspartate and alanine were also increased, which represents a protective mechanism to palliate the deleterious effects of glutamine accumulation. Both glycero-phosphocholine and *N*-acetylaspartate, markers of cell density and viability (*42*, *43*), were significantly reduced in euthyroid mice but not in hypothyroid mice after infection. This indicates again a better response against the infection in hypothyroid mice. Ketone bodies, produced from short-chain fatty acids, could be an important source of fuel for brain metabolism. The levels of 3-hydroxibutyrate increased strongly only in euthyroid mice, indicating that they respond to infection with an enhanced ketone body–based metabolism, whereas hypothyroid mice used anaerobic glycolysis and creatine pathways to obtain energy. Principal components (PC) analysis (Fig. 5B) revealed separation between infected and noninfected individuals along the second PC (PC2), which may be attributed to the influence of higher levels of lactate and glutamine in infected mice and to higher levels of glycero-phosphocholine in noninfected mice. Upon infection, euthyroid and hypothyroid mice displayed a different distribution with respect to PC1 for which acetylaspartate, alanine, acetylcarnitine, and hydroxybutyrate would be responsible. These data indicate the existence of metabolomic

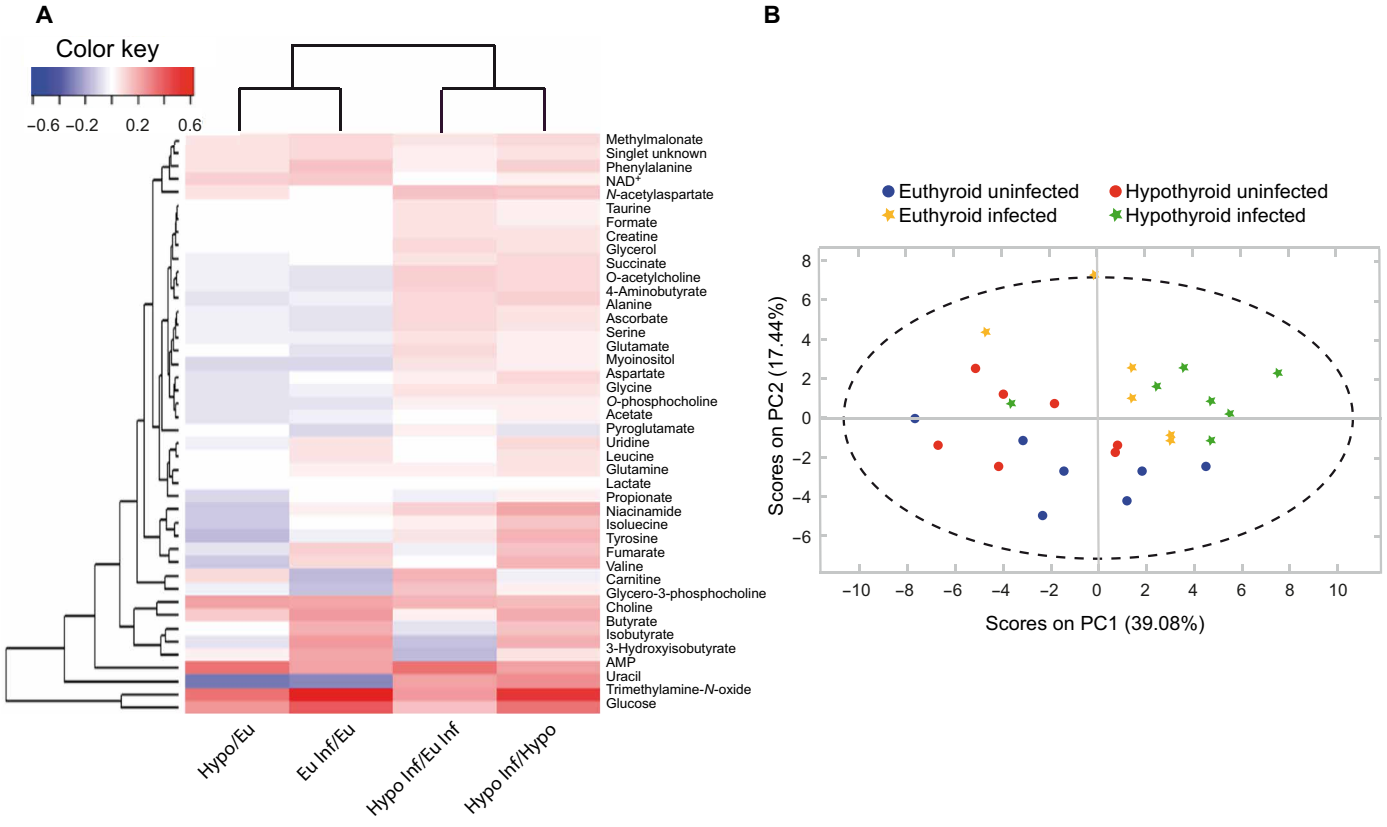


**Fig. 5. Hypothyroidism modulates the brain metabolic profile in response to PbA infection.** (**A**) Heat map analysis of nuclear MR spectroscopy metabolomics from brains of euthyroid and hypothyroid mice uninfected and at day 6 after infection ($n = 6$ to 7). (**B**) Principal components analysis (PC1 versus PC2) of the brain metabolites.

differences in the brain of euthyroid and hypothyroid mice before and during *P. berghei* infection.

## Hypothyroidism prevents behavioral and respirometric changes in ECM

Next, we evaluated how PbA infection affects global behavioral and metabolic functions in euthyroid and hypothyroid mice using respirometry cages (Fig. 6). Mice are nocturnal animals, and before the infection and during the following four nights, euthyroid mice had a much higher locomotor activity than hypothyroid mice. However, from day 4 after infection, euthyroid mice stopped moving, while the movements of hypothyroid mice were better preserved (Fig. 6A). The accumulated slope of food and drink consumption also abruptly stopped rising in infected euthyroid mice at this time, being less affected in the hypothyroid mice that are hypophagic (Fig. 6, B and C). During the first 4 days following infection, euthyroid mice showed a preserved circadian rhythm with higher nocturnal oxygen uptake ($VO_2$) and $CO_2$ output ($VCO_2$) than hypothyroid mice. However, from the fourth night, $VO_2$ and $VCO_2$ sharply decreased until death in euthyroid mice, but not in hypothyroid mice, and during these last 2 days, the situation was reversed (Fig. 6, D and E). The respiratory exchange ratio (RER; $VCO_2/VO_2$) gives an indication about the type of fuel source used. During the first four nights, euthyroid mice presented RER values above 1 and the hypothyroid mice values were somewhat lower. However, at the late stages of ECM, RER value decreased in euthyroid mice, indicating a higher rate of fat consumption, which was not so evident in infected hypothyroid mice (Fig. 6F). As expected, euthyroid mice also displayed higher energy expenditure than hypothyroid mice before and at the onset of ECM symptoms. Again, from the fourth night of infection, energy expenditure showed a marked constant decrease until death at days 6 to 7 after infection in euthyroid mice, whereas hypothyroid mice displayed more stable energy expenditure values during the course of the disease (Fig. 6G). All these data indicate that hypothyroidism confers resilience to changes in the behavioral, respirometric, and energy expenditure parameters at the late stages of the ECM (Fig. 6H).

## Regulation of ECM outcome by Sirt1 modulation

Regulation of Sirt1 activity appears to be involved in the metabolic effects of the TH (*44*). Analysis of Sirt1 protein expression in the liver, a major metabolic tissue, revealed a decrease in Sirt1 levels at day 6 after infection in both euthyroid and hypothyroid mice (fig. S13A). As a readout of Sirt1 activity, nuclear factor κB (NF-κB) p65 acetylation levels were determined (*45*). Before infection, acetyl–NF-κB p65 levels were lower in euthyroid than in hypothyroid mice. However, NF-κB p65 acetylation increased at day 6 after infection in euthyroid but not in hypothyroid mice, indicating a major decrease in Sirt1 activity during the course of PbA infection only under euthyroid conditions. This occurred despite a reduction of the total NF-κB p65 levels, which was similar in both groups of infected mice. mTORC1, another key metabolic enzyme, is also involved in the metabolic actions of the TH (*24*), and as a readout of its activity, the phosphorylation state of p70 S6K and of its substrate S6 was determined. PbA infection decreased phosphorylation of p70 S6K

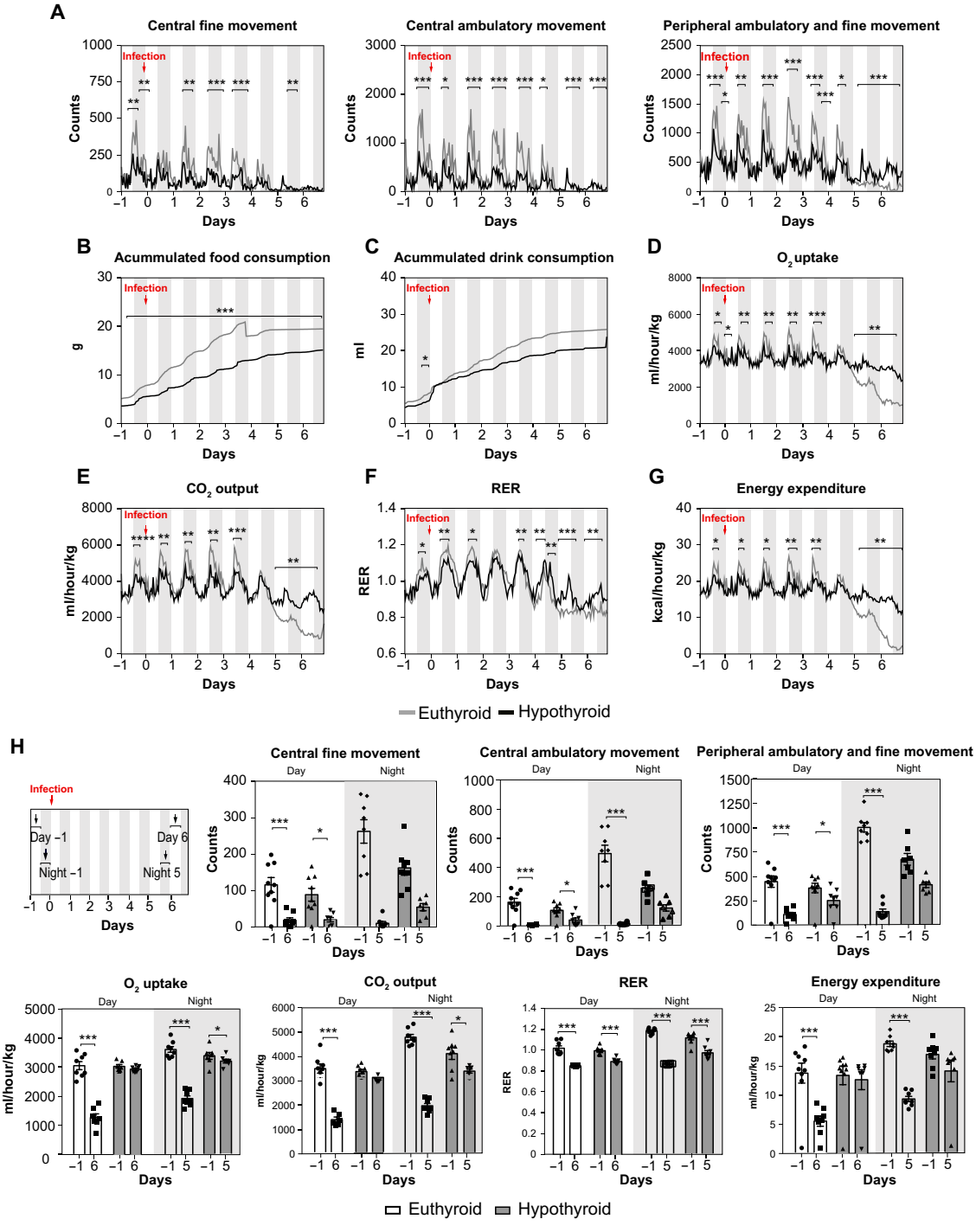


**Fig. 6. Hypothyroid mice maintain behavioral and respirometric parameters during the course of PbA infection.** (**A**) Recorded movements of euthyroid and hypothyroid mice before infection and after PbA infection. Lights are off (gray columns) between 8 p.m. and 8 a.m. and are on (white columns) otherwise. (**B** and **C**) Food and drink consumption. (**D** to **G**) $O_2$ uptake, $CO_2$ output, respiratory exchange ratio (RER), and energy expenditure ($n = 8, 7$), unpaired $t$ test. (**H**) Time diagram in which the phenomaster values were chosen for a more detailed representation of their mean values before infection and at the late ECM stage. Means ± SEM, $n = 8, 7$, one-way ANOVA followed by multiple comparisons Tukey test. $^*P < 0.05$, $^{**}P < 0.01$, and $^{***}P < 0.001$.

and S6, particularly in euthyroid mice, which showed higher phosphorylation of both proteins than hypothyroid mice (fig. S13A). Dietary restriction increases resistance to ECM by a mechanism that involves a reduction of leptin and mTORC1 activity, and administration of leptin to mice with dietary restriction decreases survival (*15*). Circulating leptin levels were significantly reduced in the hypothyroid mice and did not increase upon infection, as observed in euthyroid mice (fig. S13B). However, administration of a high dose of leptin

from day 0 of infection did not alter lethality in hypothyroid mice (fig. S13C), suggesting that hypothyroidism does not induce tolerance by a leptin-mediated mechanism. AMPK is also an essential kinase in metabolic regulation and is modulated by the TH (*23*, *46*). Both total and phosphorylated AMPK (P-AMPK) levels were higher in the hypothyroid animals before infection, but P-AMPK levels were similarly reduced in euthyroid- and hypothyroid-infected mice (fig. S13A). All these data indicate that PbA infection affects the activation state of different key enzymes involved in metabolic control and suggest that their distinct regulation in hypothyroid mice might be involved in the improved disease tolerance to ECM.

Both Sirt1 and energy expenditure displayed a major decrease in infected euthyroid mice, but not in infected hypothyroid mice. Since Sirt1 activates energy expenditure (*7*, *8*, *47*), we next analyzed the possibility that modulation of Sirt1 activity could improve tolerance to ECM. Thus, we treated euthyroid mice, starting at the day of infection, with the Sirt1 activator SRT1720 (*48*). SRT1720 treatment significantly increased survival, and about 25% of the mice never developed ECM symptoms, without altering significantly parasitemia (Fig. 7A). Treatment of infected euthyroid mice with SRT1720 resulted in reduced cerebral vessel collapse and increased CBF (Fig. 7B and movie S4), concomitantly with reduced ICP (Fig. 7C) and increased systolic blood pressure (Fig. 7D). SRT1720 also caused partial reversal of the cerebral width increase and of the cerebellum change of shape (fig. S14A), a clear improvement of the olfactory bulb damage and reduced edema in other central brain areas (fig. S14, B and C). On the other hand, inhibition of Sirt1 activity in hypothyroid mice by treatment with EX-527 (*49*) reduced survival to PbA infection, as all hypothyroid-infected mice treated with the Sirt1 inhibitor died within 5 to 10 days with ECM symptoms. EX-527 did not affect survival of uninfected hypothyroid mice (Fig. 7E). Angiographies revealed that hypothyroid-infected mice treated with EX-527 displayed increased collapse of cerebral vessels, resulting in a significant reduction of the CBF (Fig. 7F and movie S5). This was also correlated with a significant increase in ICP without a significant alteration of the systolic blood pressure (Fig. 7, G and H), with a change of cerebral and cerebellar area and thickness, suggestive of brain swelling, as well as in detectable edema in the olfactory bulb and in other central brain areas (fig. S15). These results indicate that modulation of Sirt1 activity is involved in hypothyroidism-induced tolerance to ECM and that activation of Sirt1 in euthyroid mice increases tolerance, improving the outcome of the disease.

## DISCUSSION

In this study, we proved that hypothyroidism confers disease tolerance to ECM. Without altering the pathogen load, hypothyroidism prevents the development of severe neurological symptoms and increases survival. In contrast, hyperthyroid mice die 1 day earlier than mice with normal thyroid function, further indicating that thyroidal status is an important determinant for the outcome of fatal CM.

Thyroidal dysfunction (*28*) and pituitary hyporesponsiveness (*27*) occur in patients suffering complicated malaria, suggesting that hypothalamic-pituitary thyroid axis dysregulation is involved in an emergency response to the stress situation generated by the infection. We show here that mice with CM also develop NTIS with a strong reduction of circulating TH, although the attained levels are not as low as those existing in the hypothyroid mice. According to our results, it is likely that the thyroidal dysfunction observed in the experimental murine model and in malaria patients could represent a defense mechanism trying to diminish the severity of the disease. Since millions of people live in areas of endemic iodine deficiency, which can be partially superimposed with endemic malaria, it is conceivable that the consequent hypothyroidism could confer some protection against the cerebral form of the disease. This would be reminiscent of the survival advantage that sickle human hemoglobin confers to individuals living in endemic areas of malaria (*13*), although in this case a genetic defect rather than a micronutrient deficiency would be responsible. Mice expressing sickle hemoglobin also survive to CM by a disease tolerance mechanism (*14*).

Depending on the type of pathogen, the host requires a specific metabolic state to achieve optimal disease tolerance. In a seminal study, Wang *et al.* (*50*) described opposite effects of fasting and glucose metabolism on tolerance to bacterial and viral infection in mice. Thus, glucose supplementation is detrimental in bacterial sepsis but protects against mortality in the case of viral infection. These effects are independent of the pathogen load. This is also applicable to malaria, as administration of 2-deoxyglucose increases survival against PbA (*20*), while the same compound results in strongly increased lethality in mice infected with *Plasmodium chabaudi* AJ, which causes non-CM from which most animals recover (*51*). As a previously unknown driver in developing CM, we show here the importance of TH in tolerance to PbA infection. However, accordingly, with the specific mechanisms required to attain disease tolerance to a specific pathogen, our data also show that hypothyroidism does not protect against non-CM in the experimental model of lethal infection with the *P. yoelii* YM parasite.

Hypothyroid mice displayed noticeable spleen hypoplasia before infection. However, upon malaria infection, these animals displayed marked splenomegaly with a massive increase in the number of different splenic cell populations of the three major hematopoietic lineages. At the late stage of ECM, euthyroid and hypothyroid mice reached a similar number and activation state of different splenic hematopoietic cells and showed a similar infiltration of immune cells into the brain, including $CD8^+$ T lymphocytes, which are critical in the pathogenesis of CM (*36*, *52*, *53*). Concomitantly, both types of infected mice presented BBB disruption and similar expression of PbA and cytokines in the brain at the late ECM stage. These results in hypothyroid mice are similar to those found in mice treated with 2-deoxiglucose, which survive to PbA infection despite showing BBB breakdown, nonaltered brain cytokine transcripts, and similar number and activation of the immune cells infiltrating the brain (*20*). Together, these results reinforce the idea that the protective effect of hypothyroidism against CM specifically relays in a disease tolerance mechanism that reduces brain damage. The finding that intracerebral administration of T3 to hypothyroid mice accelerates ECM development and increases mortality suggests a direct effect of the hormone on the brain parenchymal tissue.

The cause of death in CM has been attributed to brain compression and reduction of the blood flow (*39*). Brain swelling causes uncontrollable pressure that ultimately kills brainstem neurons responsible for heart and lung function, which is consistent with cerebral herniation as a cause of death (*52*). Hypothyroidism prevents the appearance of neurological symptoms, reducing the impact on brain damage, with no evident increase in ICP, brain volume, cerebellar crushing, or brainstem herniation and with no collapse of the major cerebral vessels upon PbA infection. Besides, the number of

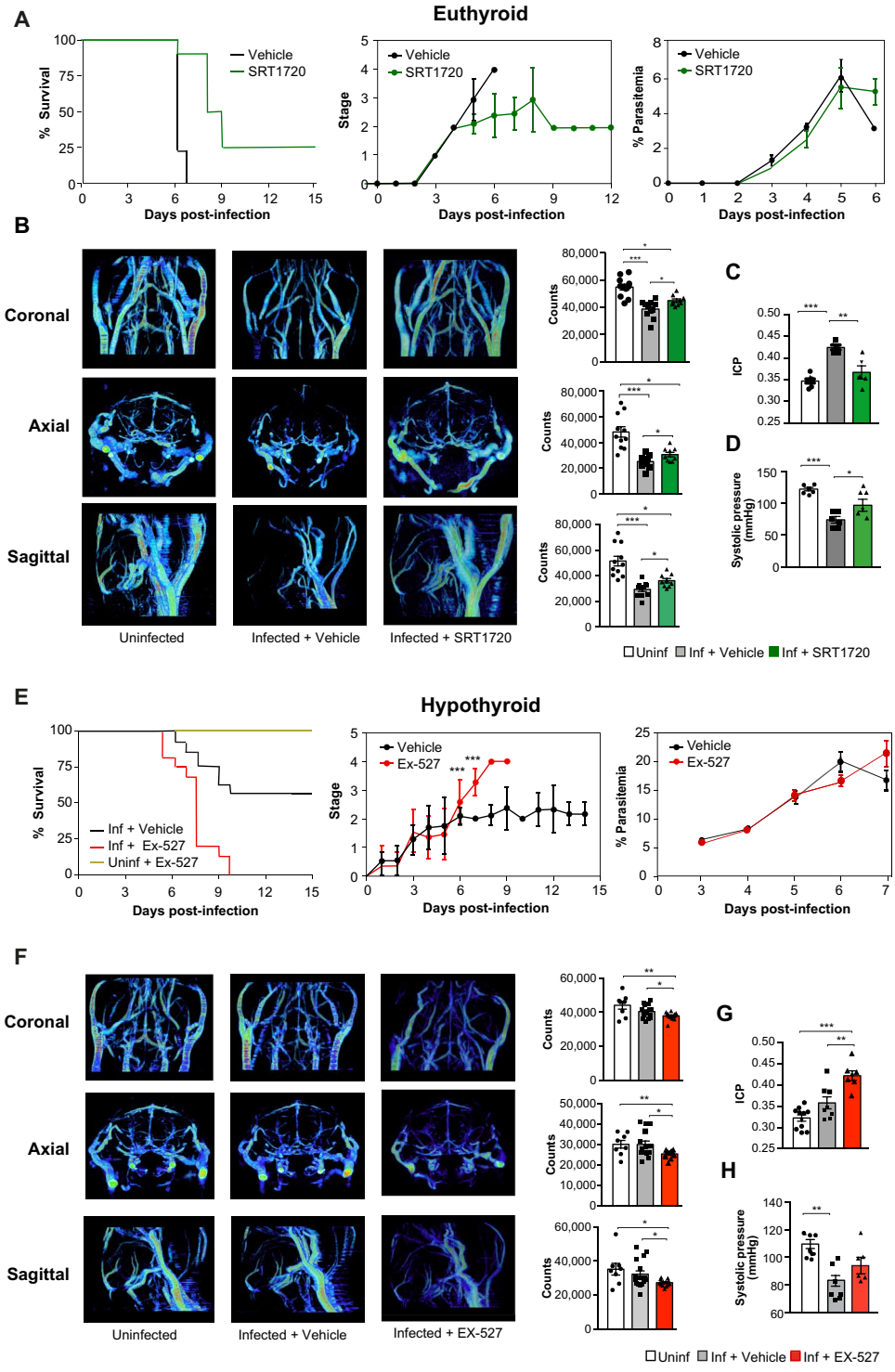


**Fig. 7. Sirt1 activity regulates ECM outcome.** (**A**) Kaplan-Meier plot, clinical stage, and parasitemia (unpaired *t* test) in euthyroid-infected mice treated daily with vehicle or with the Sirt1 activator SRT1720 from day 0 ($n = 8$). (**B**) Representative coronal, axial, and sagittal angiograms and quantifications in euthyroid uninfected (Uninf) mice and in infected (Inf) mice at day 6 after infection after the same treatments ($n = 9$ to 11). (**C**) ICP values in the same groups at day 6 after infection ($n = 5$ to 8). (**D**) Systolic blood pressure in the same animals. One-way ANOVA followed by multiple comparisons Tukey test. (**E**) Kaplan-Meier plot, clinical stage, and parasitemia in hypothyroid mice treated daily starting at day 0 of infection with vehicle or with the Sirt1 inhibitor EX-527 ($n = 17$ to 13). (**F**) Representative angiograms and quantifications in uninfected hypothyroid mice and in infected mice at day 6 after infection after the same treatments ($n = 8$ to 13). (**G**) ICP values in the same experimental groups at day 6 after infection ($n = 7$ to 11). (**H**) Systolic blood pressure in the same groups ($n = 5$ to 6). (B, C, F, and G) One-way ANOVA followed by multiple comparisons Tukey test. In all panels, error bars represent mean ± SEM. $^{*}P < 0.05$, $^{**}P < 0.01$, and $^{***}P < 0.001$.

hemorrhagic foci, other hallmark of brain damage in CM, is also significantly reduced in the infected hypothyroid mice. The sympathoadrenal system interacts with the TH at various levels (*54*), but hypothyroidism maintains the defense against ECM in adrenalectomized mice, suggesting that the protective role of hypothyroidism is independent of that system. Furthermore, hypothyroidism can be associated with arterial stiffness and secondary hypertension in humans (*55*), which in turn could reduce cerebral perfusion. However, uninfected hypothyroid mice showed decreased blood pressure, suggesting that changes in ICP, independent of peripheral blood pressure, underlie the effect of hypothyroidism in ECM. Furthermore, edema, herniation, and impaired CBF occur in infected euthyroid mice with increased ICP, but not in hypothyroid mice in which ICP does not increase upon infection, strongly suggesting that the improved survival of hypothyroid mice is a result of reduced ICP.

One of the most recognized actions of the TH is the regulation of metabolism, increasing energy expenditure (*21*, *56*). Behavioral and respirometry studies showed that, before infection and at early stages of PbA infection, hypothyroid mice display a significant reduction of energy expenditure. At later stages, only euthyroid mice, which show neurological symptoms of CM, underwent an abrupt decrease in locomotor activity, $O_2$ and $CO_2$ exchange, and energy expenditure. These changes were much less apparent in hypothyroid-infected mice. The drop in metabolic respiratory activity occurred in sick euthyroid mice without presenting a clear hypoglycemia or significant anemia, which suggests that a central respiratory failure could be the mechanism responsible and supports the idea that the metabolic state achieved under hypothyroid conditions, with lower locomotor and respiratory activity, allows the mice to display improved tolerance/resilience to the stress caused by PbA infection.

Hypothyroidism might induce tolerance to CM by altering brain metabolism, and accordingly, metabolic adaptation to infection differs between euthyroid and hypothyroid animals. Hypothyroid brains show an improved adaptive response with reduced tissue injury and protection against the deleterious effects of glutamine *(19)*. In addition, they show a shift toward a glycolitic anaerobic metabolism and to the use of creatine pathway to obtain adenosine triphosphate (ATP), while euthyroid mice respond to infection with enhanced ketone body–based metabolism. This metabolic signature shows that hypothyroidism induces a distinct metabolic status in the brains that are resistant to the damage induced by the parasite. However, it cannot be directly concluded from these results that these metabolic changes are responsible for resilience to ECM. Respirometric studies also suggest that infected euthyroid mice skew their whole-body metabolism to relay upon stored endogenous fat energy. After infection, the RER value fell to 0.8 in the euthyroid mice. A value of 1 or above indicates carbohydrate consumption, while 0.7 signifies that fat is the main fuel source.

The actions of the TH involve the regulation of key enzymes in both the brain and peripheral tissues (*22*–*24*). One of these pathways involves mTORC1, which mediates protection against CM by caloric restriction via a reduction of leptin production (*15*). Although circulating leptin levels were reduced in hypothyroid mice, leptin administration did not increase lethality in these animals, discarding this pathway as a main mediator of tolerance to CM in hypothyroidism. Sirt1 has been connected to the beneficial effects elicited by calorie restriction or fasting, increasing energy expenditure (*9*, *10*, *57*). There is a significant overlap between the actions of the TH and Sirt1 in the regulation of metabolic processes such as gluconeogenesis, fatty acid oxidation, or mitochondrial function (*25*, *58*). Our results suggest that Sirt1 activity is involved in the modulation of tolerance to CM. Treatment of hypothyroid mice with a Sirt1 inhibitor increases ICP, brain vessel compression, and lethality, while maintenance of Sirt1 activity during the course of the infection in normal animals diminishes ICP and improves CBF and survival, without significant variation in the parasitemia levels. Thus, Sirt1 activator, as well as hypothyroidism, appears to protect against ECM lethality by preventing increased ICP. However, our results do not provide the ultimate mechanism/s by which hypothyroidism preserves Sirt1 activity during infection and which are the specific cells involved. Therefore, the functional relationship between THs, Sirt1, and ECM requires further investigation.

In conclusion, our results indicate that anti-thyroidal drugs could improve the outcome of CM but hypothyroidism is harmful to health, especially in children, as THs are essential for brain development (*59*). However, the identification of Sirt1 as a mediator of the action of the TH in the outcome of CM suggests a beneficial function of Sirt1 activators for the treatment of the disease. Although hypothyroidism or Sirt1 activation rescued mice from CM, they ultimately died during the long period of anemia, probably caused by accelerated clearance of uninfected erythrocytes associated to the inability to compensate for red blood cell loss (*60*). Therefore, the use of Sirt1 activators, in combination with the drugs used to inhibit parasite replication, might be useful for the treatment of human CM, which still represents a major clinical problem in endemic countries. Most children under 5 years old presenting CM die while traveling to the nearest health care centers or within the first 24 hours of admission (*61*). Thus, we can speculate that early adjuvant therapy based on Sirt1 activators to prevent tissue and brain damage could help to reduce the high intrinsic mortality due to the disease.

## MATERIALS AND METHODS

### Mice

C57BL/6 mice from Charles River Laboratories, maintained in the animal house of the Instituto de Investigaciones Biomédicas "Alberto Sols," were used in this study. All animal experiments were done following the Institutional Animal Care and Use Committee (IACUC) guidelines in agreement with the European Community Law (86/609/EEC) and the Spanish law (R.D. 1201/2005), with approval of the Ethics Committee of the Consejo Superior de Investigaciones Científicas and Comunidad de Madrid.

### Generation of hypothyroid, euthyroid, and hyperthyroid mice

To induce hypothyroidism, 4- to 5-week-old male mice were fed with an iodine-deficient diet containing 0.15% of the antithyroidal drug propylthiouracil (E15551-04, Sniff) and with $KClO_4$ (10 g/liter) (460494, Merck) in the drinking water for 4 weeks before the experiment. Control euthyroid animals were fed with a control diet (E15552-24, Sniff), the same diet without propylthiouracil but supplemented with potassium iodide to contain 1.15 mg/kg. Mice fed with the control diet were made hyperthyroid by adding T4 (25 ng/g of mice; IRMM468, Sigma-Aldrich) and T3 (95 ng/g of mice; T-2877, Sigma-Aldrich) in the drinking water, from 14 days before infection until the end of the experiment. Drinking water was changed every day. Unless otherwise indicated, mice were maintained with the chosen diet until the end of the experiment.

### Design of the ECM model

Only 8- to 9-week-old male mice were infected with *P. berghei* strain ANKA (PbA, MRA-311, BEI Resources) or with *P. yoelii* YM (MRA755, BEI Resources), by an intraperitoneal injection of $1 \times 10^6$ infected red blood cells obtained from previously infected donor mice. Mice received food ad libitum, and drinking water was supplemented with para-amino benzoic acid at 0.05% to ensure in vivo parasite growth. Parasitemia was monitored from blood smears fixed with methanol, stained with Wright's solution (1013830500, Merck) under ×100 magnification, and calculated using Fiji program. Mice were monitored daily for clinical stage of ECM. Stages were defined by the presentation of no symptoms (0), piloerection (*1*), medium piloerection and mild ataxia (*2*), ataxia and paralysis (*3*), and convulsions and coma (*4*) (*62*). Videos of the different mice were performed with video edition software Canva. When mice showed severe ECM (stage 4), they were sacrificed by $CO_2$ asphyxiation according to ethical guidelines, and the day of death was considered to be the following day.

### Mice treatments

Euthyroid mice were injected intraperitoneally daily starting the day of the infection with the Sirt1 activator SRT1720 (HY-15145, MedChemExpress) (*48*) at a dose of 20 mg/kg in 100 µl. SRT1720 was dissolved in 10% dimethyl sulfoxide (DMSO) (D2438, Sigma-Aldrich) and 20% 2-hydroxypropyl-β-cyclodextrin (H5784, Merck) in phosphate-buffered saline (PBS). Hypothyroid mice were treated daily, starting at the day of the infection with the Sirt1 inhibitor EX-527 (E7034, Sigma-Aldrich) (*49*), at a dose of 10 mg/kg in 50 µl. EX-527 was dissolved in 4% DMSO and 10% 2-hydroxypropyl-β-cyclodextrin in PBS. In parallel, other sets of mice were treated with the corresponding vehicle without the drug. Twenty micrograms per mice of recombinant mouse leptin (498-OB, R&D Systems) dissolved in PBS was administered twice a day by intraperitoneal injection, starting the day of the infection. Five hundred microliters of mannitol (25% in 0.9% saline; Sigma-Aldrich) or vehicle (control) was daily injected in mice starting at day 0 of infection. For ICV treatment, cannulae were stereotaxically implanted into hypothyroid mice as previously described (*24*, *46*) using the following coordinates: 1.2 mm lateral to bregma, 0.6 mm posterior, 2 mm deep. Four days after implantation, animals were inoculated with PbA and T3 (16 ng in 4 µl of saline; Sigma-Aldrich) or vehicle was administered ICV daily for 6 days until the cannulae collapsed. ICV administration was performed 1 hour before turning the lights off. Adrenal glands were surgically removed from euthyroid and hypothyroid mice, and the corresponding control animals were sham-operated. The drinking water of the adrenalectomized animals was supplemented with 0.9% NaCl. Mice were allowed to recover from the surgery for 14 days before PbA inoculation.

### Hemograms

Mice were sacrificed using $CO_2$ overdose exposure, according to ethics guidelines. Blood samples were collected in EDTA tubes (1591126, EVEREST) by heart puncture. Hemograms from EDTA blood samples (400 µl) were determined at SEROLAB S.L (Madrid). Peripheral blood hemoglobin was determined by lysis of 10 µl of whole blood in 1 ml of water followed by optical density reading at 540 nm in the BioTek EL340 Microplate Reader and subsequently converted to the corresponding concentration.

### Determination of circulating cytokines

Serum plasma was obtained by centrifugation of blood samples for 5 min at 2000 rpm. Circulating cytokines were determined using the Cytokine Response Panel Kit (740622, BioLegend) according to the manufacturer's instructions, and samples were subsequently subjected to flow cytometry analysis on CytoFLEX S (Beckman and Coulter). The concentration of the different cytokines was calculated using the software LEGENDplex V8.0 supplied by BioLegend.

### Quantification of glucose and leptin

Glucose measurement was carried out in blood drops from tails using an Accu-Check Aviva detector (6453970037, Roche). Leptin levels were measured in serum samples, obtained by centrifugation of blood samples for 5 min at 2000 rpm, by using the Mouse Leptin ELISA Kit (90030, Cristalchem), following the manufacturer's instructions.

### Quantification of total circulating T3 and T4

High–specific activity $^{125}$I-T3 and $^{125}$I-T4 (3000 µCi/µg) were obtained using radioactive iodine (NEZ033A, Perkin Elmer) and (3-5)-T2 (D0629, Sigma-Aldrich) and T3 (T2877, Sigma-Aldrich) as substrates, respectively, as previously described (*63*). The separation of the labeled products was modified using ascending paper chromatography for 16 hours in the presence of butanol:ethanol:ammonia 0.5 N (5:1:2) as solvent. $^{125}$I-T3 and $^{125}$I-T4 were eluted and kept in ethanol at 4°C. TH concentration was analyzed by radioimmunoassays (RIAs) after extraction and purification of plasma samples. Briefly, tracer amounts of $^{125}$I-T3 or $^{125}$I-T4 were added to individual 80-µl aliquots of plasma and total T3 and T4 were extracted with methanol (1:6), evaporated to dryness, and dissolved in RIA buffer for determinations. The dynamic range was 0.4 to 100 pg of T3 per tube and 2.5 to 320 pg of T4 per tube. Samples were processed in duplicate, and the final results were calculated on the basis of the amount of hormone detected in the assay, the recovery of the tracers added, and the volume of the extracted plasma sample. High–specific activity $^{125}$I-T4 and $^{125}$I-T3 as well as and anti-T3 and anti-T4 antisera (originally generated by M. J. Obregon) were provided by A. Guadaño-Ferraz, IIBM.

### Identification of splenic hematopoietic cells by flow cytometry (FACS)

Splenocytes were collected and purified using a gentleMACS dissociator and Mouse Spleen Dissociation kit (130-095-926, Miltenyi), according to the manufacturer's instruction. Cell suspensions were filtered through a 70-µm cell strainer and pelleted by centrifugation at 300*g* for 5 min. To lyse erythrocytes, pelleted cells were resuspended in 1 ml of VersaLyse lysing solution (A09777, Beckman Coulter); 2 min later, 3 ml of fluorescence-activated cell sorting (FACS) buffer [PBS, 2% fetal bovine serum (FBS), and 5 mM EDTA] was added, and cells were centrifuged and washed. The different cell samples ($0.5 \times 10^6$ to $2 \times 10^6$ cells) were stained for the indicated surface markers required (see table S1) for 20 min at room temperature and subsequently washed twice with FACS buffer. For intracellular staining, cells were fixed, permeabilized with the use of a fixation/permeabilization kit (00-5523-00, Thermo Fisher Scientific), and incubated with the corresponding antibody. When possible, live and dead cells were distinguished by adding SYTOX Green (S7020, Life Technologies) or 4′,6-diamidino-2-phenylindole

(D9542, Sigma-Aldrich) 5 min before flow cytometry analysis. Unstained cells were used as a negative control to establish the flow cytometer voltage settings, and single-color positive controls were used to adjust compensation. To identify the different splenic cells, without treatment with lysis solution, cells were subjected to flow cytometry analysis as described (*32*, *64*). The absolute number of cells was calculated by adding Perfect-Count Microspheres (CYTPCM-100, Cytognos) to the flow cytometry samples. The flow cytometry data were acquired using FACSCanto II (Becton and Dickinson) or CytoFLEX S (Beckman and Coulter) and analyzed with FlowJo or CytoExpert software.

### Identification of infiltrated hematopoietic cells in brain by flow cytometry

To identify brain-infiltrated leukocytes by flow cytometry, brain samples were carefully extracted just after animal sacrifice, minced, and processed in the gentleMACS dissociator using the Adult Brain Dissociation Kit (130-107-677, Miltenyi). Samples were subsequently filtered through a 70-μm cell strainer, and cells were centrifuged in a 36% Percoll gradient (P1644, Sigma-Aldrich)/Dulbecco's modified Eagle's medium–Hepes (DF-041, Sigma-Aldrich), enriched with 10% FBS (10270-106, Gibco) and 0.4% Hanks' balanced salt solution (14185-045, Gibco) for 30 min at 800*g* at room temperature. Erythrocytes were lysed in 400 μl of VersaLyse lysing solution (A09777, Beckman Coulter), as described above, and cells were stained for the indicated surface markers (see table S1). Cell number determination and FACS analysis were performed as described above.

### Systolic blood pressure

Blood pressure was measured by tail-cuff plethysmography. For this, animals were trained for 1 week before initial blood pressure measurements and 1 day before PbA infection. Then, blood pressure was measured at day 6 after infection in the BP-2000 Blood Pressure Analysis System (Visitech Systems, USA). Measurements were done always at the same time of the day from 8 a.m. to 10 a.m. At least 10 individual observations were performed and averaged for each animal.

### Brain-blood barrier permeability

Mice were injected intravenously through the retro-orbital venous sinus with 100 μl of Evans blue (E2129, Sigma-Aldrich) diluted at 10 mg/ml in PBS, at day 6 after infection. After 1 hour, brains were extracted, weighted, and incubated in formamide (295876, Sigma-Aldrich) at 37°C for 2 days. Absorbance was measured spectrophotometrically in the BioTek 340 Microplate Reader at 620 nm, and data were corrected by brain weight.

### Histopathological studies

Brains and spleens were removed without any perfusion. Spleen and one cerebral hemisphere for each animal were fixed in 4% buffered formalin (141328, PanReac AppliChem) during 72 hours. Coronal sections were embedded in paraffin wax (253211, PanReac AppliChem). Serial 5-μm sections were stained with H&E (75290, PanReac AppliChem; 4530, Merck). The number of hemorrhages was quantified using Fiji ImageJ software (*65*). Hemorrhages were estimated using a Max-Entropy thresholding method for the eosin intensity values, determined by the "Colour deconvolution" tool and posteriorly visually identified and revised in the original image for each section. The area of the brain tissue in each section was also quantified using Fiji ImageJ software, using an Otsu thresholding method of the 8-bit image. Data collected from quantification of the sections for each mouse were expressed as the number of microhemorrhages per square millimeter of cerebral tissue.

### Western blot analysis

Mouse livers were homogenized in ice with cold lysis buffer [50 mM Hepes (3375 Sigma-Aldrich), 1% Triton X-100 (T8787, Sigma-Aldrich), 50 mM sodium pyrophosphate tetrabasic (P8010, Sigma-Aldrich), 0.1 mM sodium fluoride (S7920, Sigma-Aldrich), 10 mM EDTA (E9884, Sigma-Aldrich), 10 mM sodium orthovanadate (S6508, Sigma-Aldrich), and 1:100 protease inhibitor mix (GE80-6501-23, GE Healthcare, pH 7.5)]. Samples were centrifuged at 14,000 rpm for 30 min at 4°C, the supernatant was collected, and protein concentration was measured using the Pierce BCA Protein Assay Kit (23227, Thermo Fisher Scientific). Protein samples (30 to 50 μg) were diluted with lysis buffer (20 μl per sample). After the addition of 2× Laemmli buffer (S3401, Sigma-Aldrich), samples were boiled for 5 min and loaded onto 4 to 15% SDS–polyacrylamide gel electrophoresis (4561086, Bio-Rad) gel gradient, together with protein molecular weight standard (B4MWP03, Cultek). Gels were transferred to polyvinylidene difluoride membranes (IPVH00010, Merck Millipore), subsequently incubated with the corresponding primary antibodies, and developed with an anti-rabbit peroxidase-labeled antibody or with anti-mouse peroxidase-labeled antibody (see table S1). Blots were imaged using medical x-ray films blue (Agfa) in a medical film processor (model SRX-101A, Konica) and analyzed by quantitative densitometry using ImageJ software. Protein levels were normalized with respect to β-tubulin, used as a loading control.

### Quantitative real-time PCR assays

Tissue from liver, brain, and spleen was frozen immediately after dissection and homogenized in RNase-Free Disposable Pellet Pestles (16339635, Fisher Scientific). RNA was extracted with TRI Reagent Solution (AM9738, Invitrogen) and quantified in NanoDrop ND-100 (Thermo Fisher Scientific). One microgram of RNA was treated with RNase-Free DNase (79254, Qiagen), and cDNA synthesis was performed with the iScript cDNA Synthesis Kit (170-8891, Bio-Rad) with oligo-dT and Random hexamer primers in a reaction protocol of 5 min at 25°C, 30 min at 42°C, and 5 min at 85°C. Quantitative polymerase chain reaction (PCR) was performed with Fast SYBR Green Master Mix (4385612, Applied Biosystems) on a Stratagene Mx3005P Real-Time PCR machine with the primers shown in table S2. The thermal cycling conditions used were activation of the polymerase at 95°C for 20 s, 40 cycles of denaturation at 95°C for 3 s, and annealing and extend step at 60°C for 30 s. Data analysis was done using the comparative cycle threshold ($C_T$) method, and transcripts were normalized to the internal control hypoxanthine-guanine phosphoribosyltransferase (HPRT).

### Analysis of mice behavioral and respirometric parameters

Respiratory and metabolic analysis was performed at the animal facility of the IIBM (Madrid, Spain). Metabolic parameters were measured using a 16-chamber TSE Phenomaster monitoring system (TSE Systems GmbH, Bad Homburg, Germany). Animals were placed into the Phenomaster room 72 hours before the onset of the experiment to ensure a correct adaption. Then, mice were housed

individually in cages and, 48 hours later, inoculated with PbA. Data on food and water consumption, energy expenditure, periphery and central movements, $VO_2$, and $VCO_2$ were captured every hour during 8 days and stored using the TSE Phenomaster software. Respiratory exchange rate (RER) corresponds to coefficient $VCO_2$/$VO_2$, and energy expenditure was calculated as (3.185 + 1.232 × RER) × $VO_2$. Day was considered between 8 a.m. and 8 p.m. when lights are on.

### Magnetic resonance imaging

MRI experiments were performed at the High Field Magnetic Resonance Imaging Service (IIBM, Madrid, Spain; www.iib.uam.es/portal/web/siermac). MRI acquisitions were performed on a Bruker BioSpec MRI system (Bruker Medical GmbH, Ettlingen, Germany) using a 7.0-T horizontal-bore superconducting magnet, equipped with a $^1$H selective birdcage resonator of 23 mm and a Bruker gradient insert with 90 mm of diameter (maximum intensity, 36 G/cm). The animals were first placed in an anesthesia induction chamber with 3% IsoFlo (Ecuphar) and pure oxygen as carrier gas at a flow rate of 0.8 liter min$^{-1}$ for 4 min. Subsequently, anesthetized animals were placed on the bed of the MRI system. All data were acquired using a Hewlett-Packard console running ParaVision 7 software (Bruker Medical GmbH) operating on a Linux platform. The mice, placed into the center of the volume radio frequency coil and positioned in the magnet, were under continuous inhalation of anesthesia via a nose cone with a mask connected to the anesthetic gas maintained between 1.5 and 2% IsoFlo with the help of the spectrometer to maintain the respiratory cycle between 60 and 80 beats per minute. The temperature of the animal was maintained with a recirculating water bed at 37°C, and its physiological status was monitored using the BioTrig physiological monitoring system (SA Instruments, Stony Brook, NY), which displays the respiratory cycle and body temperature. T1-weighted (T1W) spin-echo anatomical images were acquired with a multislice multiecho sequence and the following parameters: repetition time (TR) = 350 ms; echo time (TE) = 10 ms; averages (Av) = 3; field of view (FOV) = 2.3 cm; acquisition matrix = 256 × 256 corresponding to an in-plane resolution of 89 × 89 μm$^2$; slice thickness = 1.00 mm; and number of slices = 14 axial, 10 sagittal, and 6 coronal. T2W spin-echo anatomical images were acquired with a rapid acquisition with relaxation enhancement (RARE) sequence and the following parameters: TR = 2500 ms; TE = 26 ms; RARE factor = 8; Av = 4; FOV = 2.3 cm; acquisition matrix = 256 × 256 corresponding to an in-plane resolution of 89 × 89 μm$^2$; slice thickness = 1.00 mm; and number of slices = 14 axial, 10 sagittal, and 6 coronal. Angiograms were acquired with two-dimensional (2D) gradient echo time-of-flight sequence MR angiography without contrast agent and displayed in maximum intensity projection with the following parameters: TR = 15 ms, TE = 2.6 ms, TR = 15 ms, FA (flip angle) = 80°, 160 slices of 0.3 mm without gap, matrix = 256 × 256, and FOV = 38 × 38 mm. Angiography images were obtained from a 3D construction made with ImageJ with the effect "Thermal Lut." Data were quantified using the same brightness threshold parameters for all animals. Angiography videos were performed with Fiji program, treated all with the same brightness/contrast parameters. BBB permeability was assessed by contrast-enhanced T1W imaging and axial images, which were taken 15 min after intraperitoneal injection of gadolinium–diethylenetriamine pentaacetic acid (0.3 mmol/kg, Magnevist, Bayer Health Care Pharmaceuticals). 2D-axial T1W precontrast and postcontrast images were used to calculate gadolinium enhancement maps. The index was calculated as the difference between the postcontrast and precontrast image signal divided by the precontrast image signal in a pixel-by-pixel way, and the mean value of different brain structures was computed. Brain volume was calculated as the summation of the volumes of all the T1 axial and midsagittal slices with ImageJ. Two researchers measured independently the brain surface and distances from mid-sagittal images with ImageJ and RadiAnt DICOM Viewer software. Brain surface was calculated using the length between the olfactory bulb and the posterior end of the cerebellum and from the brain height stemming from the pituitary gland.

### Intracranial pressure

ICP was determined measuring the optic nerve sheath diameter in T2-weighted coronal MRI images (*40*), with slice thickness of 1.00 mm, in both eyes, and the mean value was calculated.

### Brain $^1$H-NMR spectrophotometry metabolomic analysis

Brain samples, lyophilized and pulverized (50 mg of dry brain), were shipped on dry ice to Biosfer Teslab (Reus, Spain; https://biosferteslab.com) for the analysis by nuclear magnetic resonance (NMR) spectroscopy. Tissue samples were homogenized by ultrasonication during 10 min. Aqueous extracts were obtained from the brain tissue using the 1-butanol:methanol method (*66*) with slight modifications. BUME was optimized for batch extractions with di-isopropyl ether replacing heptane as the organic solvent, and the aqueous phase was subjected to three subsequently lipid extraction cycles. Aqueous extracts were recovered and completely dried in SpeedVac until evaporation of organic solvents and frozen at −80°C until $^1$H-NMR analysis. Aqueous extracts were reconstituted in deuterated PBS containing 2.32 mM trimethylsilyl propionate and transferred to 5-mm NMR glass tubes. $^1$H-NMR spectra were measured at 600.20 MHz using an Avance III-600 Bruker spectrometer. 1D $^1$H pulse experiments were carried out using the nuclear Overhauser effect spectroscopy presaturation sequence to suppress the residual water peak at around 4.7 parts per million for aqueous extracts. For the analysis of the metabolites, the NMR area associated with the concentration of each metabolite was obtained after the spectral analysis by using an in-house line-shape fitting based on algorithm developed to deconvolute the preprocessed NMR spectra by using Lorentzian and Gaussian functions to minimize the fitting error (*43*). The NMR areas were transformed into concentration units by using specific conversion factors depending on the proton numbers of the molecular structure generating the signal and a trimethylsilylpropanoic acid internal standard as previously described (*42*). Each metabolite was identified by checking for all its resonances along the spectra and then quantified using line-shape fitting methods on one of its signals.

### Statistical analysis

Two-tailed Student's *t* tests were used for comparisons between two groups. One-way analysis of variance (ANOVA) with post hoc Tukey test was used to compare all pairs of columns from at least three different groups, and survival curves were analyzed with Kaplan-Meier test. The results are always expressed as means ± SEM. $P < 0.05$ was considered statistically significant. The significance of ANOVA posttest or the Student's *t* test in the experimental groups indicated in the figures is shown as $^*P < 0.05$, $^{**}P < 0.01$, and $^{***}P < 0.001$. Statistics was performed with GraphPad Prism 7.0 software.

## SUPPLEMENTARY MATERIALS

Supplementary material for this article is available at https://science.org/doi/10.1126/sciadv.abj7110

View/request a protocol for this paper from *Bio-protocol*.

## REFERENCES AND NOTES


1. I. N. Nkumama, W. P. O'Meara, F. H. A. Osier, Changes in malaria epidemiology in Africa and new challenges for elimination. *Trends Parasitol.* **33**, 128–140 (2017).
2. S. C. Wassmer, G. E. Grau, Severe malaria: What's new on the pathogenesis front? *Int. J. Parasitol.* **47**, 145–152 (2017).
3. A. G. Craig, G. E. Grau, C. Janse, J. W. Kazura, D. Milner, J. W. Barnwell, G. Turner, J. Langhorne; on behalf of the participants of the Hinxton Retreat meeting on "Animal Models for Research on Severe Malaria", The role of animal models for research on severe malaria. *PLOS Pathog.* **8**, e1002401 (2012).
4. J. S. Ayres, D. S. Schneider, Tolerance of infections. *Annu. Rev. Immunol.* **30**, 271–294 (2012).
5. M. P. Soares, L. Teixeira, L. F. Moita, Disease tolerance and immunity in host protection against infection. *Nat. Rev. Immunol.* **17**, 83–96 (2017).
6. S. Weis, A. R. Carlos, M. R. Moita, S. Singh, B. Blankenhaus, S. Cardoso, R. Larsen, S. Rebelo, S. Schäuble, L. D. Barrio, G. Mithieux, F. Rajas, S. Lindig, M. Bauer, M. P. Soares, Metabolic adaptation establishes disease tolerance to sepsis. *Cell* **169**, 1263–1275.e14 (2017).
7. A. S. Banks, N. Kon, C. Knight, M. Matsumoto, R. Gutiérrez-Juárez, L. Rossetti, W. Gu, D. Accili, SirT1 gain of function increases energy efficiency and prevents diabetes in mice. *Cell Metab.* **8**, 333–341 (2008).
8. C. Canto, K. J. Menzies, J. Auwerx, NAD(+) metabolism and the control of energy homeostasis: A balancing act between mitochondria and the nucleus. *Cell Metab.* **22**, 31–53 (2015).
9. L. Bordone, L. Guarente, Calorie restriction, SIRT1 and metabolism: Understanding longevity. *Nat. Rev. Mol. Cell Biol.* **6**, 298–305 (2005).
10. R. H. Houtkooper, E. Pirinen, J. Auwerx, Sirtuins as regulators of metabolism and healthspan. *Nat. Rev. Mol. Cell Biol.* **13**, 225–238 (2012).
11. D. G. Hardie, F. A. Ross, S. A. Hawley, AMPK: A nutrient and energy sensor that maintains energy homeostasis. *Nat. Rev. Mol. Cell Biol.* **13**, 251–262 (2012).
12. R. A. Saxton, D. M. Sabatini, mTOR signaling in growth, metabolism, and disease. *Cell* **169**, 361–371 (2017).
13. T. N. Williams, T. W. Mwangi, S. Wambua, T. E. A. Peto, D. J. Weatherall, S. Gupta, M. Recker, B. S. Penman, S. Uyoga, A. Macharia, J. K. Mwacharo, R. W. Snow, K. Marsh, Negative epistasis between the malaria-protective effects of alpha+−thalassemia and the sickle cell trait. *Nat. Genet.* **37**, 1253–1257 (2005).
14. A. Ferreira, I. Marguti, I. Bechmann, V. Jeney, Â. Chora, N. R. Palha, S. Rebelo, A. Henri, Y. Beuzard, M. P. Soares, Sickle hemoglobin confers tolerance to Plasmodium infection. *Cell* **145**, 398–409 (2011).
15. P. Mejia, J. H. Treviño-Villarreal, C. Hine, E. Harputlugil, S. Lang, E. Calay, R. Rogers, D. Wirth, M. T. Duraisingh, J. R. Mitchell, Dietary restriction protects against experimental cerebral malaria via leptin modulation and T-cell mTORC1 suppression. *Nat. Commun.* **6**, 6050 (2015).
16. O. C. Oliveira-Lima, N. L. Almeida, C. M. Almeida-Leite, J. Carvalho-Tavares, Mice chronically fed a high-fat diet are resistant to malaria induced by Plasmodium berghei ANKA. *Parasitol. Res.* **118**, 2969–2977 (2019).
17. V. Zuzarte-Luis, J. Mello-Vieira, I. M. Marreiros, P. Liehl, A. F. Chora, C. K. Carret, T. Carvalho, M. M. Mota, Dietary alterations modulate susceptibility to *Plasmodium* infection. *Nat. Microbiol.* **2**, 1600–1607 (2017).
18. L. Vandermosten, T. T. Pham, S. Knoops, C. de Geest, N. Lays, K. van der Molen, C. J. Kenyon, M. Verma, K. E. Chapman, F. Schuit, K. de Bosscher, G. Opdenakker, P. E. van den Steen, Adrenal hormones mediate disease tolerance in malaria. *Nat. Commun.* **9**, 4525 (2018).
19. E. B. Gordon, G. T. Hart, T. M. Tran, M. Waisberg, M. Akkaya, A. S. Kim, S. E. Hamilton, M. Pena, T. Yazew, C. F. Qi, C. F. Lee, Y. C. Lo, L. H. Miller, J. D. Powell, S. K. Pierce, Targeting glutamine metabolism rescues mice from late-stage cerebral malaria. *Proc. Natl. Acad. Sci. U.S.A.* **112**, 13075–13080 (2015).
20. A. Wang, S. C. Huen, H. H. Luan, K. Baker, H. Rinder, C. J. Booth, R. Medzhitov, Glucose metabolism mediates disease tolerance in cerebral malaria. *Proc. Natl. Acad. Sci. U.S.A.* **115**, 11042–11047 (2018).
21. R. Mullur, Y. Y. Liu, G. A. Brent, Thyroid hormone regulation of metabolism. *Physiol. Rev.* **94**, 355–382 (2014).
22. B. Cannon, J. Nedergaard, Thyroid hormones: Igniting brown fat via the brain. *Nat. Med.* **16**, 965–967 (2010).
23. N. Martinez-Sanchez, P. Seoane-Collazo, C. Contreras, L. Varela, J. Villarroya, E. Rial-Pensado, X. Buqué, I. Aurrekoetxea, T. C. Delgado, R. Vázquez-Martínez, I. González-García, J. Roa, A. J. Whittle, B. Gomez-Santos, V. Velagapudi, Y. C. L. Tung, D. A. Morgan, P. J. Voshol, P. B. Martínez de Morentin, T. López-González, L. Liñares-Pose, F. Gonzalez, K. Chatterjee, T. Sobrino, G. Medina-Gómez, R. J. Davis, N. Casals, M. Orešič, A. P. Coll, A. Vidal-Puig, J. Mittag, M. Tena-Sempere, M. M. Malagón, C. Diéguez, M. L. Martínez-Chantar, P. Aspichueta, K. Rahmouni, R. Nogueiras, G. Sabio, F. Villarroya, M. López, Hypothalamic AMPK-ER stress-JNK1 axis mediates the central actions of thyroid hormones on energy balance. *Cell Metab.* **26**, 212–229.e12 (2017).
24. L. Varela, N. Martínez-Sánchez, R. Gallego, M. J. Vázquez, J. Roa, M. Gándara, E. Schoenmakers, R. Nogueiras, K. Chatterjee, M. Tena-Sempere, C. Diéguez, M. López, Hypothalamic mTOR pathway mediates thyroid hormone-induced hyperphagia in hyperthyroidism. *J. Pathol.* **227**, 209–222 (2012).
25. R. A. Sinha, B. K. Singh, P. M. Yen, Direct effects of thyroid hormones on hepatic lipid metabolism. *Nat. Rev. Endocrinol.* **14**, 259–269 (2018).
26. E. Fliers, A. Boelen, An update on non-thyroidal illness syndrome. *J. Endocrinol. Invest.* **44**, 1597–1607 (2021).
27. T. M. Davis, W. Supanaranond, S. Pukrittayakamee, S. Krishna, G. R. Hart, J. M. Burrin, S. Looareesuwan, N. Vilaiwanna, N. J. White, The pituitary-thyroid axis in severe falciparum malaria: Evidence for depressed thyrotroph and thyroid gland function. *Trans. R. Soc. Trop. Med. Hyg.* **84**, 330–335 (1990).
28. L. Wartofsky, D. Martin, J. M. Earll, Alterations in thyroid iodine release and the peripheral metabolism of thyroxine during acute falciparum malaria in man. *J. Clin. Invest.* **51**, 2215–2232 (1972).
29. J. L. Gorstein, J. Bagriansky, E. N. Pearce, R. Kupka, M. B. Zimmermann, Estimating the health and economic benefits of universal salt iodization programs to correct iodine deficiency disorders. *Thyroid* **30**, 1802–1809 (2020).
30. M. J. Berry, A. L. Kates, P. R. Larsen, Thyroid hormone regulates type I deiodinase messenger RNA in rat liver. *Mol. Endocrinol.* **4**, 743–748 (1990).
31. H. A. Del Portillo, M. Ferrer, T. Brugat, L. Martin-Jaular, J. Langhorne, M. V. G. Lacerda, The role of the spleen in Malaria. *Cell. Microbiol.* **14**, 343–355 (2012).
32. A. Sanchez, M. C. Orizaola, D. Rodríguez-Muñoz, A. Aranda, A. Castrillo, S. Alemany, Stress erythropoiesis in atherogenic mice. *Sci. Rep.* **10**, 18469 (2020).
33. D. Kimura, M. Miyakoda, K. Kimura, K. Honma, H. Hara, H. Yoshida, K. Yui, Interleukin-27-producing CD4(+) T cells regulate protective immunity during Malaria parasite infection. *Immunity* **44**, 672–682 (2016).
34. E. Belnoue, M. Kayibanda, J. C. Deschemin, M. Viguier, M. Mack, W. A. Kuziel, L. Rénia, CCR5 deficiency decreases susceptibility to experimental cerebral malaria. *Blood* **101**, 4253–4259 (2003).
35. G. S. Campanella, A. M. Tager, J. K. El Khoury, S. Y. Thomas, T. A. Abrazinski, L. A. Manice, R. A. Colvin, A. D. Luster, Chemokine receptor CXCR3 and its ligands CXCL9 and CXCL10 are required for the development of murine cerebral malaria. *Proc. Natl. Acad. Sci. U.S.A.* **105**, 4814–4819 (2008).
36. A. Haque, S. E. Best, K. Unosson, F. H. Amante, F. de Labastida, N. M. Anstey, G. Karupiah, M. J. Smyth, W. R. Heath, C. R. Engwerda, Granzyme B expression by CD8+ T cells is required for the development of experimental cerebral malaria. *J. Immunol.* **186**, 6148–6156 (2011).
37. M. F. Penet, A. Viola, S. Confort-Gouny, Y. le Fur, G. Duhamel, F. Kober, D. Ibarrola, M. Izquierdo, N. Coltel, B. Gharib, G. E. Grau, P. J. Cozzone, Imaging experimental cerebral malaria in vivo: Significant role of ischemic brain edema. *J. Neurosci.* **25**, 7352–7358 (2005).
38. H. Zhao, T. Aoshi, S. Kawai, Y. Mori, A. Konishi, M. Ozkan, Y. Fujita, Y. Haseda, M. Shimizu, M. Kohyama, K. Kobiyama, K. Eto, J. Nabekura, T. Horii, T. Ishino, M. Yuda, H. Hemmi, T. Kaisho, S. Akira, M. Kinoshita, K. Tohyama, Y. Yoshioka, K. J. Ishii, C. Coban, Olfactory plays a key role in spatiotemporal pathogenesis of cerebral malaria. *Cell Host Microbe* **15**, 551–563 (2014).
39. K. B. Seydel, S. D. Kampondeni, C. Valim, M. J. Potchen, D. A. Milner, F. W. Muwalo, G. L. Birbeck, W. G. Bradley, L. L. Fox, S. J. Glover, C. A. Hammond, R. S. Heyderman, C. A. Chilingulo, M. E. Molyneux, T. E. Taylor, Brain swelling and death in children with cerebral malaria. *N. Engl. J. Med.* **372**, 1126–1137 (2015).
40. T. Geeraerts, V. F. J. Newcombe, J. P. Coles, M. Abate, I. E. Perkes, P. J. A. Hutchinson, J. G. Outtrim, D. A. Chatfield, D. K. Menon, Use of T2-weighted magnetic resonance imaging of the optic nerve sheath to detect raised intracranial pressure. *Crit. Care* **12**, R114 (2008).
41. C. A. Okoromah, B. B. Afolabi, E. C. Wall, Mannitol and other osmotic diuretics as adjuncts for treating cerebral malaria. *Cochrane Database Syst. Rev.* **2011**, CD004615 (2011).
42. S. Ghosh, A. Sengupta, S. Sharma, H. M. Sonawat, Metabolic fingerprints of serum, brain, and liver are distinct for mice with cerebral and noncerebral malaria: A $^{1}$H NMR spectroscopy-based metabonomic study. *J. Proteome Res.* **11**, 4992–5004 (2012).
43. A. S. Sheikh, S. A. Sheikh, M. A. Mohamed, Changes in brain metabolites in experimental cerebral malaria infection with Plasmodium berghei ANKA: A literature review. *J. Pak. Med. Assoc.* **64**, 1179–1185 (2014).
44. B. K. Singh, R. A. Sinha, P. M. Yen, Novel transcriptional mechanisms for regulating metabolism by thyroid hormone. *Int. J. Mol. Sci.* **19**, (2018).
45. F. Yeung, J. E. Hoberg, C. S. Ramsey, M. D. Keller, D. R. Jones, R. A. Frye, M. W. Mayo, Modulation of NF-kappaB-dependent transcription and cell survival by the SIRT1 deacetylase. *EMBO J.* **23**, 2369–2380 (2004).

46. M. Lopez, L. Varela, M. J. Vázquez, S. Rodríguez-Cuenca, C. R. González, V. R. Velagapudi, D. A. Morgan, E. Schoenmakers, K. Agassandian, R. Lage, P. B. M. de Morentin, S. Tovar, R. Nogueiras, D. Carling, C. Lelliott, R. Gallego, M. Oresic, K. Chatterjee, A. K. Saha, K. Rahmouni, C. Diéguez, A. Vidal-Puig, Hypothalamic AMPK and fatty acid metabolism mediate thyroid regulation of energy balance. *Nat. Med.* **16**, 1001–1008 (2010).
47. P. Bai, C. Canto, A. Brunyánszki, A. Huber, M. Szántó, Y. Cen, H. Yamamoto, S. M. Houten, B. Kiss, H. Oudart, P. Gergely, J. Menissier-de Murcia, V. Schreiber, A. A. Sauve, J. Auwerx, PARP-2 regulates SIRT1 expression and whole-body energy expenditure. *Cell Metab.* **13**, 450–460 (2011).
48. L. B. Gano, A. J. Donato, H. M. Pasha, C. M. Hearon Jr., A. L. Sindler, D. R. Seals, The SIRT1 activator SRT1720 reverses vascular endothelial dysfunction, excessive superoxide production, and inflammation with aging in mice. *Am. J. Physiol. Heart Circ. Physiol.* **307**, H1754–H1763 (2014).
49. W. Xian, T. Li, L. Li, L. Hu, J. Cao, Maresin 1 attenuates the inflammatory response and mitochondrial damage in mice with cerebral ischemia/reperfusion in a SIRT1-dependent manner. *Brain Res.* **1711**, 83–90 (2019).
50. A. Wang, S. C. Huen, H. H. Luan, S. Yu, C. Zhang, J.-D. Gallezot, C. J. Booth, R. Medzhitov, Opposing effects of fasting metabolism on tissue tolerance in bacterial and viral inflammation. *Cell* **166**, 1512–1525.e12 (2016).
51. K. Cumnock, A. S. Gupta, M. Lissner, V. Chevee, N. M. Davis, D. S. Schneider, Host energy source is important for disease tolerance to Malaria. *Curr. Biol.* **28**, 1635–1642.e3 (2018).
52. P. A. Swanson II, G. T. Hart, M. V. Russo, D. Nayak, T. Yazew, M. Pena, S. M. Khan, C. J. Janse, S. K. Pierce, D. B. McGavern, CD8+ T cells induce fatal brainstem pathology during cerebral Malaria via luminal antigen-specific engagement of brain vasculature. *PLOS Pathog.* **12**, e1006022 (2016).
53. A. Villegas-Mendez, R. Greig, T. N. Shaw, J. B. de Souza, E. Gwyer Findlay, J. S. Stumhofer, J. C. R. Hafalla, D. G. Blount, C. A. Hunter, E. M. Riley, K. N. Couper, IFN-γ–producing $CD4^+$ T cells promote experimental cerebral malaria by modulating $CD8^+$ T cell accumulation within the brain. *J. Immunol.* **189**, 968–979 (2012).
54. J. E. Silva, S. D. Bianco, Thyroid-adrenergic interactions: Physiological and clinical implications. *Thyroid* **18**, 157–165 (2008).
55. I. Saito, K. Ito, T. Saruta, Hypothyroidism as a cause of hypertension. *Hypertension* **5**, 112–115 (1983).
56. B. Kim, Thyroid hormone as a determinant of energy expenditure and the basal metabolic rate. *Thyroid* **18**, 141–144 (2008).
57. H. C. Chang, L. Guarente, SIRT1 and other sirtuins in metabolism. *Trends Endocrinol. Metab.* **25**, 138–145 (2014).
58. S. Thakran, P. Sharma, R. R. Attia, R. T. Hori, X. Deng, M. B. Elam, E. A. Park, Role of sirtuin 1 in the regulation of hepatic gene expression by thyroid hormone. *J. Biol. Chem.* **288**, 807–818 (2013).
59. I. Velasco, S. C. Bath, M. P. Rayman, Iodine as essential nutrient during the first 1000 days of life. *Nutrients* **10**, 290 (2018).
60. K. J. Evans, D. S. Hansen, N. van Rooijen, L. A. Buckingham, L. Schofield, Severe malarial anemia of low parasite burden in rodent models results from accelerated clearance of uninfected erythrocytes. *Blood* **107**, 1192–1199 (2006).
61. A. Dzeing-Ella, P. C. Nze Obiang, R. Tchoua, T. Planche, B. Mboza, M. Mbounja, U. Muller-Roemer, J. Jarvis, E. Kendjo, E. Ngou-Milama, P. G. Kremsner, S. Krishna, M. Kombila, Severe falciparum malaria in Gabonese children: Clinical and laboratory features. *Malar. J.* **4**, 1 (2005).
62. M. Linares, P. Marín-García, S. Pérez-Benavente, J. Sánchez-Nogueiro, A. Puyet, J. M. Bautista, A. Diez, Brain-derived neurotrophic factor and the course of experimental cerebral malaria. *Brain Res.* **1490**, 210–224 (2013).
63. M. J. Obregon, G. Morreale de Escobar, F. Escobar del Rey, Concentrations of triiodo-L-thyronine in the plasma and tissues of normal rats, as determined by radioimmunoassay: Comparison with results obtained by an isotopic equilibrium technique. *Endocrinology* **103**, 2145–2153 (1978).
64. A. Sanchez, C. Contreras-Jurado, D. Rodríguez, J. Regadera, S. Alemany, A. Aranda, Hematopoiesis in aged female mice devoid of thyroid hormone receptors. *J. Endocrinol.* **244**, 83–94 (2020).
65. J. Schindelin, I. Arganda-Carreras, E. Frise, V. Kaynig, M. Longair, T. Pietzsch, S. Preibisch, C. Rueden, S. Saalfeld, B. Schmid, J. Y. Tinevez, D. J. White, V. Hartenstein, K. Eliceiri, P. Tomancak, A. Cardona, Fiji: An open-source platform for biological-image analysis. *Nat. Methods* **9**, 676–682 (2012).
66. L. Lofgren, G. B. Forsberg, M. Stahlman, The BUME method: A new rapid and simple chloroform-free method for total lipid extraction of animal tissue. *Sci. Rep.* **6**, 27688 (2016).


**Acknowledgments:** We thank T. N. Herrán (IIB) for NMR data acquisition, C. Palomo (UAM) for histological preparations, and L. Molero (UAM) for flow cytometry assistance. **Funding:** This work was funded by grants SAF2017-83289-R to S.A. and A.A., SAF2017-90604REDT to A.A., and BIO2016-77430-R to J.M.B. from the Ministerio de Economía y Competitividad; B2017/BMD-3724 to S.A. and A.A. from the Comunidad de Madrid; and CIBERONC CB/16/00228 to A.A. from the Instituto de Salud Carlos III. **Author contributions:** Conceptualization, writing—original draft, project administration, and funding acquisition: A.A. and S.A. Investigation: D.R.-M., Á.S., S.P.-B., C.C.-J., A.M.-P., M.T.-C., M.G.-H., R.R.-D., and C.F. Formal analysis: D.C., E.F.-V., I.M.-C., I.C.-C., and J.R. Supervision: J.M.B., A.M.B., and G.S. Writing—review and editing: A.A. and S.A. **Competing interests:** The authors declare that they have no competing interests. **Data and materials availability:** All data needed to evaluate the conclusions in the paper are present in the paper and/or the Supplementary Materials.

Submitted 27 May 2021
Accepted 11 February 2022
Published 6 April 2022
10.1126/sciadv.abj7110